

# Significant and megathrust earthquake predictions by real-time monitoring of the genesis processes with Physical Wavelets

Fumihide Takeda<sup>1,2,\*</sup>

<sup>1</sup> Takeda Engineering Consultant Co., 2-14-23 Ujina Miyuki Minamiku, Hiroshima, Japan

<sup>2</sup> Earthquake Prediction Institute at Imabari, 3-4-56 Go-Shin-Yashiki-Cho, Imabari, Japan

\* f\_takeda@tec21.jp

Real-time monitoring of significant and megathrust earthquake genesis processes over a few months with Physical Wavelets suggests the predictability of the focuses, fault movements, sizes, and rupture times within a day accuracy.

## Contents

Contents.....	1
Abstract .....	2
1 Introduction.....	2
2 A virtual EQ particle's stochastic motion .....	3
3 Physical Wavelets .....	3
4 Significant EQ genesis processes and predictions .....	4
4.1 Oscillatory CQK and CQT.....	4
Figure 1. CQK and CQT.....	5
Figure 2. CQKD and CQTD .....	7
4.2 Particular time $\tau_a$ , $\tau_b$ , and $\tau_r$ .....	7
4.3 Equations for fault movement, size, and magnitude .....	7
4.4 Equations for rupture time .....	8
4.5 Equations for the focus.....	9
4.6 Real-time monitoring of CQK and CQT .....	9
4.7 GPS observation of CQK and CQT processes with $PW(c, j)$ .....	9
5 Megathrust EQ genesis processes and predictions .....	9
5.1 CQK and CQT processes.....	9
5.2 GPS observations .....	10
Figure 3. GPS stations, vertical co-seismic displacement, foreshocks, and aftershocks of the M9 EQ .....	12
5.3 Bulge deformation.....	13
Figure 4. Three phases of crustal deformation (a megathrust EQ genesis process) .....	14
Figure 5. The bulge and M9 observations at Onagawa station (east coast) .....	17
5.4 Abnormal movements of the oceanic plate and real-time monitoring .....	17

Table 1 (Abnormal motion of the subducting northwestern Pacific Plate).....	18
Figure 6. The abnormal westward motion at Chichijima station.....	21
Figure 7. $D(E, \tau) - A(E, \tau)$ path for Fig. 6b .....	24
6 Automatic detection of anomalies.....	25
7 A strain-energy cycle during the significant and megathrust EQ genesis processes.....	26
Figure 8. Normalized strain-energy cycle on the 1995 Kobe M7.2.....	27
Figure 9. Normalized strain-energy cycle on the 2011 Tohoku M9.....	28
Concluding summary .....	28
Acknowledgments.....	30
References .....	30
Appendix .....	33
Figure A1. Foreshocks and aftershocks of the 2011 Tohoku M9 EQ.....	33

## Abstract

Japan's 20 km-mesh seismograph network has observed the significant and megathrust earthquake (EQ) genesis processes with Physical Wavelets, suggesting the predictability of the focuses, fault movements, sizes, and rupture times a few months before the events rupture. Similarly, the Japanese Global Positioning System (GPS) observed the 2011 Tohoku megathrust EQ genesis process with Physical Wavelets, suggesting the predictability of the EQ and tsunami two months before the events. Their time-prediction accuracies are within a day by real-time monitoring of the expected rupture processes, like heavy rain and typhoon disaster prevention warnings. Physical Wavelets analyze the stochastic or noisy non-differentiable time series data observed by each network and describe the equations of the EQ genesis processes in real time for the predictions.

## 1 Introduction

The Earth's lithosphere is a three-layer system of the brittle (B) upper crust, the ductile (D) lower crust, and the D uppermost mantle. The plate-driving forces create steady-state creep in the D parts, which builds up the stress in the B part through the D-B transition region by coupling the three layers [1]. If the ductile strain rate is high, the creep deformation generates EQs of various sizes in the B upper crust. The regional stress state is a so-called frictional failure whose principal stress components are vertical and horizontal to the Earth's surface [1]. The seismic activities appear stochastic and complex. A self-organizing system [2] or a self-organized criticality (SOC) hypothesis [3] may account for the complexity. However, the hypothesis fails to explain the 2011 Tohoku M9 EQ genesis process observed with Japanese seismic and GPS networks [4–8]. Furthermore, the well-known EQ size-frequency distributions of foreshocks, a mainshock, and aftershocks show a subtle depth dependence originating from the D-B transition region [7]. The depth dependence contradicts the expected scale-invariance (self-similarity) [9, 10] and the SOC hypothesis [3].

Physical Wavelets describe the scale dependence as an equation of how the principal stress changes generate significant EQs and megathrust EQs in every mesh size of about  $4^\circ$  by  $5^\circ$  in longitude and latitude throughout Japan [6,

[7](#), [11–14](#)]. The equation in each mesh describes the consecutive EQ events as a virtual EQ particle motion of the unit mass under the crustal stress changes. The mesh size and shape are selective, and it may be a small or large region covered by a seismic network [\[6\]](#)

## 2 A virtual EQ particle's stochastic motion

Each EQ event in a mesh detected by the seismic network has the property of the focus (in latitude  $LAT$ , longitude  $LON$ , and depth  $DEP$ ), its origin time (event time), and magnitude  $MAG$ . They are the so-called EQ source parameters. The interval between consecutive event times is the inter-event interval ( $INT$ ), reflecting the stress state [\[15\]](#). In the  $c$ -coordinate space ( $c = LAT, LON, DEP, INT$ , and  $MAG$ ), an event is a virtual EQ particle of unit mass that emerges in the space. At the next EQ event, the particle moves to a new location. The movement discontinuously changes direction and speed like a Brownian particle [\[16\]](#). Each  $c$ -component is a zigzagged non-time differentiable pathway [\[6, 7, 11–14\]](#);

$$\{c\} = \{d(c,1), d(c,2), \dots, d(c,m), \dots, d(c,N)\}. \quad (1)$$

The  $d(c, m)$  is the  $c$ -coordinate of the EQ particle's position at time  $m$ . The time is the chronological event index  $m$  ( $m \geq 1$  because there is no  $INT$  at  $m = 0$ ). The  $d(c, N)$  is the last observed EQ position. Denote a reference position, or a mean of  $d(c, m)$  averaged over  $N$  by  $\langle d(c, m) \rangle_N$ , and the relative change from each reference,  $d(c, m) - \langle d(c, m) \rangle_N$ , by  $d(c, m)$ . Thus,  $\{c\}$  may be a displacement time series from each reference. Index time  $m$  is not a stochastic quantity. A selection of  $MAG \geq Mc$  ( $Mc \approx 3.5$ ) for every mesh shows that  $d(c, m)$  is a function of the principal stress components having a reduced stochastic noise level of about 15 ~ 25 % [\[7\]](#).

After every main event, each noisy displacement  $d(c, m)$  shows exponential growth, named a Lyapunov exponent. The most prominent of all exponents, the largest exponent, is statistically distinct from surrogates created by randomly shuffling the chronological index  $m$  in  $\{c\}$ , suggesting the significant event is deterministic chaos [\[7, 13\]](#). The deterministic evidence buried in  $\{c\}$  is an enlarged memory of the significant event revealed with the Hurst exponents [\[7\]](#). The evidence suggests some physical models exist on significant and megathrust EQ generations. However, the models found in seismic catalogs are all statistical, like the Omori law on the cumulative aftershocks [\[17\]](#), epidemic-type aftershock sequences (ETAS) [\[18, 19\]](#), and their asymmetry behavior [\[20\]](#).

The magnitude selection with  $MAG \geq Mc$  ( $Mc \approx 3.5$ ) shows position  $d(c, m)$  having depth-dependent frequency-size distributions for  $M = d(MAG, m)$  and  $t = d(INT, m)$  [\[7\]](#). Physical Wavelets [\[6–8\]](#) expect to observe similar scale-dependent seismogenic structures and processes of a radius of 120 km [\[21–24\]](#). At present, any other tool cannot locate and extract the scale-dependent evolution of the principal stress components to significant and megathrust EQs.

## 3 Physical Wavelets

Taking a moving average of  $2w + 1$  events ( $w \geq 1$ ) of Eq. (1), the  $c$ -coordinate of the smoothed displacement at time  $\tau$  is then,

$$D(c, \tau) = [1 / (2w + 1)] \sum_{m=-w}^w d(c, \tau + m). \quad (2)$$

Physical Wavelets replace a time differentiation of  $D(c, \tau)$  by taking the difference at  $s$  event separation ( $s \geq 2w + 1$ ). Velocity  $V(c, \tau)$  and acceleration  $A(c, \tau)$  are then,

$$V(c, \tau) = [D(c, \tau + s/2) - D(c, \tau - s/2)] / s \quad (3)$$

and

$$\begin{aligned} A(c, \tau) &= [V(c, \tau + s/2) - V(c, \tau - s/2)] / s \\ &= [D(c, \tau + s) - 2D(c, \tau) + D(c, \tau - s)] / s^2. \end{aligned} \quad (4)$$

The time-reversal operation is to change  $\tau$  to  $-\tau$ , for which  $D(c, \tau)$ ,  $V(c, \tau)$ , and  $A(c, \tau)$  have the properties of  $D(c, -\tau) = D(c, \tau)$ ,  $V(c, -\tau) = -V(c, \tau)$ , and  $A(c, -\tau) = A(c, \tau)$ . Thus, they have the time differential properties on the differentiable  $D(c, \tau)$  and  $V(c, \tau)$  [6–8]. The relationships between  $D(c, \tau)$ ,  $V(c, \tau)$ , and  $A(c, \tau)$  at time  $\tau$  are the equations of the EQ particle's average motion, defined for the stochastic or non-differentiable time series  $\{c\}$  with Physical Wavelets. The EQ particle's stochastic motion may carry the periodically fluctuating components embedded in  $\{c\}$ . The extraction of specific fluctuations is significant if the mutual correlation between Physical Wavelets and  $\{c\}$  is high. In the fluctuation (frequency  $f$  in 1/events) domain, the extracting function is a low-pass filter in  $D(c, \tau)$ , a bandpass filter in  $V(c, \tau)$ , and another bandpass filter in  $A(c, \tau)$ . The cut-off frequencies are respectively  $(4s)^{-1}$  and  $(4s/3)^{-1}$  for high-pass and low-pass filters [6–8]. Thus,  $A(c, \tau)$  oscillates with a periodic frequency component of  $f \approx (2s)^{-1}$ , extracted from time series  $\{c\}$ . We note that time  $\tau$  lags from the current time  $j$  because  $\tau = j - w - s$ . Thus, real-time observation of the EQ average motion is at time  $j = \tau + w + s$ .

## 4 Significant EQ genesis processes and predictions

### 4.1 Oscillatory CQK and CQT

With a selection of  $MAG \geq Mc$  ( $Mc \approx 3.5$ ) in a small mesh of about  $4^\circ$  by  $5^\circ$  in longitude and latitude, the EQ particle motion, averaged over  $2w + 1$  events ( $w \approx 7 \sim 17$ ), is under a restoring force of  $F(c, \tau) \propto A(c, \tau) \approx -K(c) \times D(c, \tau)$  [6, 7]. Each  $A(c, \tau)$  has a periodicity of about  $2s$ . The positive constant  $K(c)$  is a weak function of time  $\tau$ . The  $A(c, \tau)$  and  $D(c, \tau)$  are the functions of noise-free three principal stress components. As the EQ average movement approaches an imminent significant EQ,  $A(c, \tau)$  among  $c = DEP$ ,  $INT$ , and  $MAG$  establishes two phase-inversions between oscillatory  $A(DEP, \tau)$  and  $A(INT, \tau)$  with the negative amplitude of  $A(MAG, \tau)$  [6, 7, 11–14]. An inversion with positive  $A(INT, \tau)$  and negative  $A(DEP, \tau)$  is CQK, named after the 1995 Kobe M 7.2, as in Fig. 1. Another inversion with negative  $A(INT, \tau)$  and positive  $A(DEP, \tau)$  is CQT after the 2000 Tottori M 7.2. The CQ stands for Critical Quiescence, K for Kobe, and T for Tottori. The CQK and CQT in  $D(c, \tau)$  are CQKD and CQTD, as in Fig. 2. The significant EQ having CQK or CQT ruptures in the periodic motion with the expected EQ source parameters; focus, fault movement, size, and rupturing event time  $m$  [6, 7, 11–14]. The real-time monitoring of strain-energy cycles in section 7 converts the event index time to the rupturing date and time [6, 7, 11–14]. Almost every significant EQ and swarm ( $M >$  about 6) shows either CQK or CQT throughout meshes in Japan, including the 2011 Tohoku M9 with CQK [6]. A few exceptions exist to the significant EQs with the preceding medium-size swarms ( $M \approx 5$ ) that masked CQK or CQT [6]. However, resizing the mesh reveals the CQK or CQT and even detects the medium-size swarms as an isolated CQT process. The EQ swarms in a mesh are all CQTs [6].



The CQK and CQT have seismogenic structures with upward (to the Earth's surface) and downward stress loading to the hanging wall at fault surfaces, respectively [6, 7]. The CQKs are all in the low Coda Q spots, whereas the CQTs are in the high Coda Q spots throughout the Coda Q map of Japan [6, 25].

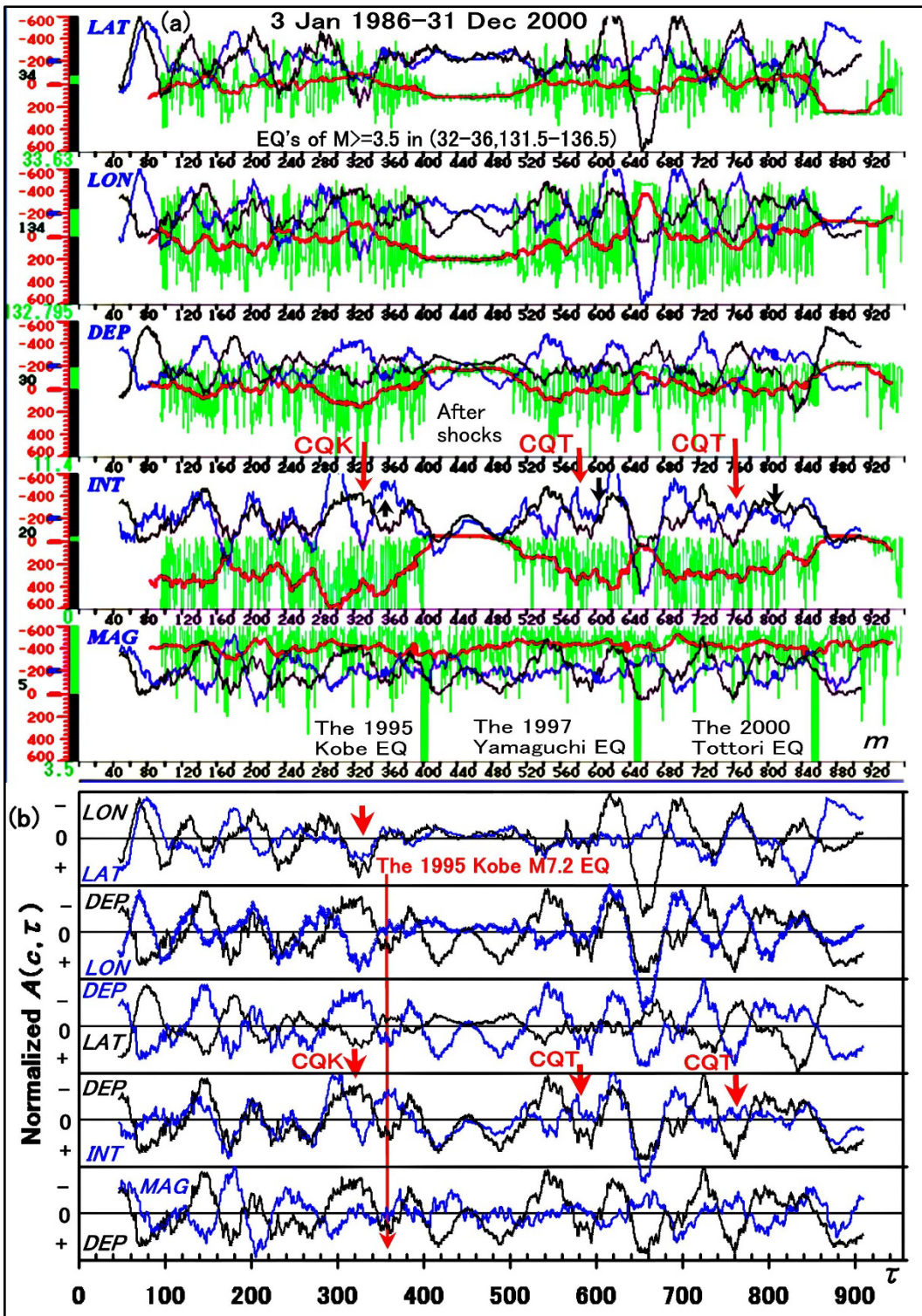
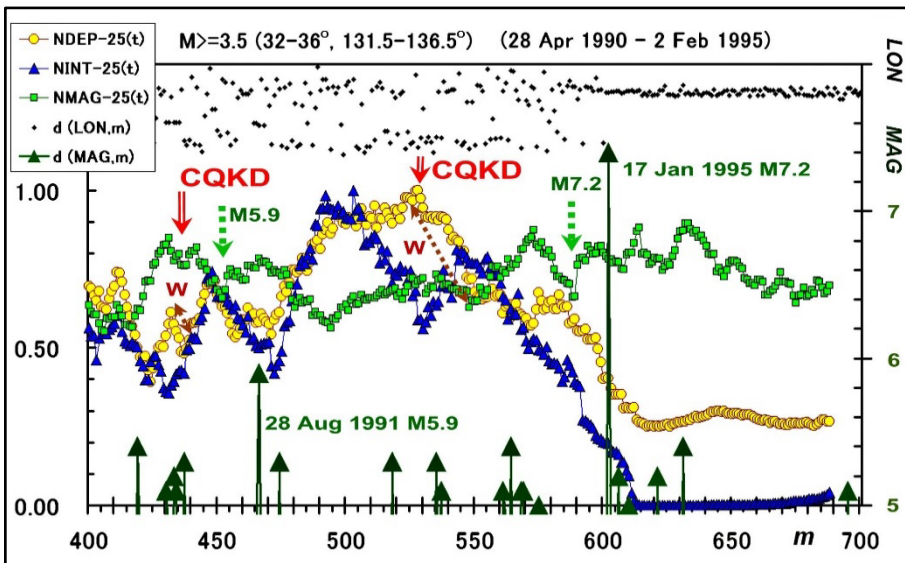


Figure 1. CQK and CQT

Modified and reproduced from references [6, 7]. (a) An EQ particle motion with  $MAG \geq 3.5$  and  $DEP \leq 300$  km in a small mesh region of  $LAT = 32^\circ-36^\circ$  N and  $LON = 131.5^\circ-136.5^\circ$  E. The shallow particle motion in the EQ  $c$  coordinate space whose  $c$  axis is the vertical axis of  $LAT$ ,  $LON$ ,  $DEP$ ,  $INT$ , and  $MAG$  on the left. All the horizontal scales are in chronological event index  $m$ , which

shares other time  $t$  and  $\tau$  where  $m = t + w$  and  $t = \tau + s$  ( $w = 12$  and  $s = 35$ ). The date at  $m = 0$  and 1 is 3 Jan 1986 and 5 Jan 1986, respectively. The  $d(c, m)$  in green is the relative position from each graphical reference of  $34^\circ$  N,  $133^\circ$  E, 30 km, 20 hours, and 5. They are all at zeroes of the manometer-like scales on the left. The scale magnification is 200 times for  $LAT$  and  $LON$ , 10 times for  $DEP$ , 2 times for  $INT$ , and 400 times for  $MAG$ . For example, the  $LAT$ ,  $LON$ , and  $DEP$  at scale  $-200$  correspond to  $33^\circ$  N,  $132^\circ$  E, and 10 km, respectively. The  $MAG$  range is from 3.5 ( $-600$ ) to 6.5 (600), so it saturates above 6.5. Each manometer column shows a variation of  $d(c, m)$  with its digital reading during monitoring. The last readings at  $m = 956$  (31 Dec 2000) are  $LAT = 33.63^\circ$  N,  $LON = 132.795^\circ$  E,  $DEP = 11.4$  km,  $INT = 0$  (0.2165) hours, and  $MAG = 3.5$ . The positive direction is downward from each reference point. The relative position  $D(c, t)$  and acceleration  $A(c, \tau)$  show the periodic fluctuations of about 70 (2s) events. The  $D(c, t)$  is red, and  $A(c, \tau)$  is blue and black. From the top axis, the black  $A(c, \tau)$  is  $c = LON, DEP, LAT, DEP,$  and  $DEP$ . Their relative amplitudes are from each origin of the blue bar marked at  $-200$  on the left scale. The  $d(c, m)$ ,  $D(c, t)$ , and  $A(c, \tau)$  become bold at the events of  $MAG \geq 6$ . The bold lines of  $d(MAG, m)$  with black arrows have the EQ names of the 1995 Kobe M7.2 (at  $m = 402$ , 17 Jan 1995), the 1997 Yamaguchi M6.6 (at  $m = 649$ , 25 Jun 1997), and the 2000 Tottori M7.2 (at  $m = 856$ , 6 Oct 2000). The black arrows on  $A(INT, \tau)$  point to their temporal locations. (b) Normalized pair of  $A(c, \tau)$ . Each pair of blue and black  $A(c, \tau)$  is normalized to its maximum  $A(c, \tau)$  in the  $-$  region. Thus, every amplitude of  $A(c, \tau) < 0$  is within  $-$  one. The first and last 47 events for  $A(c, \tau)$  are not obtained because of  $m = \tau + s + w$  ( $w = 12$  and  $s = 35$ ). The 1995 Kobe M7.2 EQ is at the long-downward arrow. The short arrows in  $DEP-INT$  row are at CQK and CQT. Blue  $A(LAT, \tau)$  and black  $A(LON, \tau)$ , pointed to by another short arrow above CQK, show  $A(LON, \tau) > A(LAT, \tau) > 0$ .

(a)



(b)

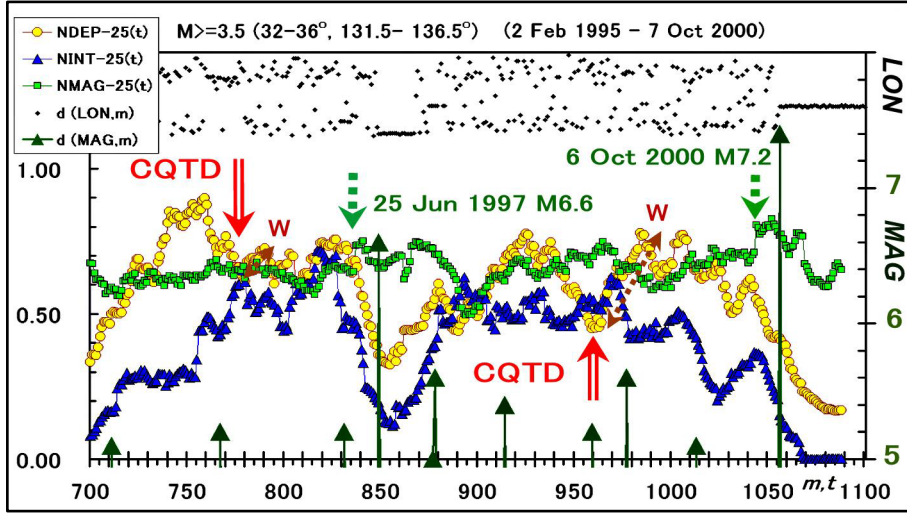


**Figure 2. CQKD and CQTD**

Modified and reproduced from references [6, 7]. (a) The CQKD of  $D(DEP, t)$ ,  $D(INT, t)$ , and  $[D(MAG, t) - 3]$  with  $2w + 1 = 25$  events in Eq. (2) are normalized to NDEP-25(t), NINT-25(t) and NMAG-25(t) with the past maximum values of 47.16 km, 331.33 h, and 1.4, respectively. At the Kobe CQKD of  $t = 528$  (28 Jun 1993),  $D(DEP, t)$ ,  $D(INT, t)$ , and  $D(MAG, t)$  are 47.16 km, 195.48 h, and 4.0, respectively. The  $MAG$  scales of  $d(MAG, m)$  are on the right, for which  $MAG \geq 5$  is in up-arrows. The  $d(LON, m)$  is relative on the righthand scale. Index  $m = 1$  starts on 8 Jan 1983, not 5 Jan 1986, as in Fig. 1a. The 1995 Kobe event in dot-arrow is at  $t = 590$  ( $m = 602$ ). The fault width  $W$  is on a depth segment of NDEP-25(t). The estimated  $W = 20$  km is in section 4.3. Figure part (a) shows that the M5.9 with  $w = 5.9$  km is at  $t = 454$  ( $m = 466$ , 26 Aug 1991). The  $D(DEP, t)$  oscillation at the CQKD has about 14-event periodicity that the  $A(DEP, \tau)$  of 70-event periodicity filtered out, resulting in  $A(DEP, \tau)$  and  $A(INT, \tau)$  in phase. Thus, we do not observe the M5.9 CQK [6]. (b) The CQTD for the 1997 Yamaguchi M6.6 (moment magnitude  $M_W = 5.9$ ,  $W = 5.5$  km) is at  $t = 837$  ( $m = 849$ , 25 Jun 1997), and the 2000 Tottori M7.2 ( $M_W = 6.8$ ,  $W = 15$  km) is at  $t = 1044$  ( $m = 1056$ , 6 Oct 2000).

#### 4.2 Particular time $\tau_a$ , $\tau_b$ , and $\tau_r$

The particular time  $\tau_a$ ,  $\tau_b$ , and  $\tau_r$  are for  $c = INT$  and  $DEP$  during CQK and CQT [6, 7]. Time  $\tau_a$  is at the first positive (or negative)  $A(c, \tau)$  peak amplitude. The  $\tau_b$  is when  $A(c, \tau)$  is zero after the first peak. The  $\tau_r$  is at the second  $A(c, \tau)$  peak. The imminent significant event ruptures at time  $\tau_r$  for  $c = INT$  or  $DEP$ , as in Fig. 1 [6, 7, 11–14]. Unlike perfect inversions of CQK (the 1995 Kobe M7.2) and CQT (the 2004 Chuetsu M6.8 [6]), there are partial phase inversions between  $A(INT, \tau)$  and  $A(DEP, \tau)$ . For such cases, some  $\tau_r$  has a delay to the third  $A(c, \tau)$  peak [6]. To predict the expected peak in  $A(c, \tau)$  at current time  $j$  where time  $\tau = j - w - s$ , we use the periodicity in  $A(c, \tau)$ , or we locate a sharp change in  $D(c, \tau)$  that will expect a peak in  $A(c, \tau)$  because of time  $\tau = j - w$  for  $D(c, \tau)$  [6].

#### 4.3 Equations for fault movement, size, and magnitude

We assume a significant EQ has a fault plane of width  $W$  and length  $L$  in km. The restoring force  $F(c, \tau)$  with  $c = LAT, LON$ , and  $DEP$  generates the shear stress exceeding the critical failure value of the fault plane during CQK or CQT [6, 7]. The horizontal force components to the Earth's surface are  $F(LAT, \tau_a)$  and  $F(LON, \tau_a)$ . The expected fault length  $L$  has the components  $D(LAT, \tau_a)$  and  $D(LON, \tau_a)$  in degrees [7]. The vertical force component with  $F(DEP, \tau_a) < 0$  is upward (to the Earth's surface) for CQK. The  $F(DEP, \tau_a) > 0$  is downward (from the Earth's surface) for CQT. Figure 2 shows an example of expected fault width  $W \approx |D(DEP, \tau_a)|$  [6, 7].



As for the 1995 Kobe M7.2 CQK, the horizontal force points clockwise  $60^\circ$  from N (north) because  $F(LAT, \tau a)$  and  $F(LON, \tau a)$  are proportional to  $(LAT, LON) = (0.25^\circ, 0.53^\circ)$  [7]. The  $F(DEP, \tau a)$  points upward. An arrow in Fig. 1b also shows a magnitude relation of  $A(LON, \tau) > A(LAT, \tau) > 0$  during the entire CQK, suggesting the net force direction of about  $68^\circ (= 45^\circ + 45^\circ / 2)$  clockwise from N. Thus,  $F(c, \tau a)$  will induce the shear stress to move the hanging wall toward the net force direction in a right-lateral strike-slip with an upward dip-slip component. The Kobe EQ focal mechanism had (Strike, Dip, Rake) =  $(233^\circ, 86^\circ, 167^\circ)$  [26, 27]. The  $167^\circ$  rake indicates that the shear stress moved the hanging wall opposite the strike at  $53^\circ (= 233^\circ - 180^\circ)$  clockwise from N, having  $66^\circ (= 233^\circ - 167^\circ)$  clockwise from N and upward by  $13^\circ$  relative to the reference strike. The observation supports the expected fault movement by  $F(c, \tau a)$ . Furthermore, the displaced magnitudes are  $|D(DEP, \tau a)| = 20$  km,  $|D(LAT, \tau a)| = |-0.25^\circ|$  and  $|D(LON, \tau a)| = |-0.53^\circ|$ , having the total length of 56.4 km in harmony with the aftershock distribution of  $W = 20$  km and  $L = 77$  km [28].

The 1997 Yamaguchi M6.6 (at  $m = 649$ , 25 Jun 1997, in Fig. 1) had CQT having the focal mechanism of (Strike, Dip, Rake) =  $(55^\circ, 83^\circ, -153^\circ)$  [27]. The hanging wall slipped opposite the reference strike at  $235^\circ$  clockwise from N, having  $208^\circ (= 55^\circ + 153^\circ)$  clockwise from N with a downward dip-slip of  $27^\circ$  relative to the reference. The  $A(LON, \tau a) \approx A(LAT, \tau a) < 0$  at  $\tau a$  from  $A(DEP, \tau a)$  in Fig. 1b suggests the net force direction of  $225^\circ (= 180^\circ + 45^\circ)$  clockwise from N to move the hanging wall. Figure 2b shows  $W \approx |D(DEP, \tau a)| = 5.5$  km. The aftershock distribution was  $(W, L) = (10$  km, 10km) [29].

Similarly, the 2000 Tottori M7.2 (at  $m = 856$ , 6 Oct 2000, in Fig. 1) was CQT with (Strike, Dip, Rake) =  $(145^\circ, 71^\circ, -11^\circ)$  [27]. The focal mechanism shows the hanging wall slipped toward the reference strike of  $145^\circ$  clockwise from N, having  $156^\circ$  clockwise from N with a downward dip-slip of  $11^\circ$  from the reference. The  $A(LON, \tau a) \approx A(LAT, \tau a) < 0$  at  $\tau a$  of  $A(INT, \tau a)$  suggests the net force pointing clockwise  $225^\circ$  from N moved the hanging wall, different from the slip direction. However, a sharp transition from  $A(LON, \tau a) \approx A(LAT, \tau a) < 0$  to  $A(LON, \tau) > 0$  and  $A(LAT, \tau) \approx 0$  for  $\tau a < \tau < \tau r$  suggests the net force clockwise direction from N is  $90^\circ \sim 225^\circ$ , which covers the slip direction of  $145^\circ$ . The fault width  $W$  in Fig. 2b shows  $|D(DEP, \tau a)| = 15$  km in harmony with the aftershock distribution of  $(W, L) = (15$ km, 30km) [30].

The observed length  $L$  and width  $W$  in km during CQK and CQT become an imminent EQ's planar-fault size. The significant EQ's magnitude can be estimated by an empirical  $M = \log S + 3.9$  ( $S = L \times W$ ) [17]. As for the Kobe CQK observation, the predicted  $M$  is 6.9. The seismological observation of  $M$  is 6.9 and 7.2 for the moment and the JMA magnitude [31], respectively. The estimation of JMA's  $M$  with an assumption of  $L = 2W$  ( $W \approx |D(DEP, \tau a)|$ ) agrees with the observed  $M$  for most significant events throughout Japan [6].

#### 4.4 Equations for rupture time

The  $D(INT, \tau r)$  and  $A(INT, \tau r)$  show an expected rupture-time  $\tau r$  in  $m = \tau r + s + w$  within one or two event time accuracy [6, 7, 11–14]. For example, the Kobe CQK showed  $\tau r = 19$  events on 24 Oct 1994 [6, 7]. The Kobe EQ event ruptured in 19 events on 17 Jan 1995. The  $D(DEP, \tau r)$  and  $A(DEP, \tau r)$  may replace the corresponding  $D(INT, \tau r)$  and  $A(INT, \tau r)$  to predict the rupture time. The conversion from the event time  $\tau r$  to the date and time requires an average rate of events obtained by a strain energy cycle in section 7 [6, 7].

Some CQK events, having a significant upward dip-slip component and  $MAG < \text{about } 6$ , have considerable time delays from the expected rupture-time  $\tau r$ . The delay is due to the fault failure's insufficient upward share stress loading. Thus, another upward loading at a new  $\tau r$  of oscillatory CQK is necessary [6]. Other CQK events have  $MAG \approx 6$  during

the CQK process, and then CQT follows. The 2003 Off-Tokachi megathrust M8 EQ was such a case, and the M8 EQ ruptured at time  $\tau$  of CQT [13].

The final rupture time prediction becomes within a day accuracy by real-time monitoring of the strain energy accumulation and release cycles, as in section 7.

#### 4.5 Equations for the focus

As for the equation of focus during CQK and CQT, the  $A(c, t)$  with  $c = LAT, LON,$  and  $DEP$  may make the corresponding  $D(c, t)$  have the most straightforward linear extrapolations to the expected rupture-time  $\tau$  [6, 7, 11–14]. For example, the linear prediction shows  $(34.53^\circ, 135.18^\circ, 20.8 \text{ km})$  in  $(LAT, LON, DEP)$  for the Kobe EQ, which matches the  $(34.595^\circ, 135.038^\circ, 16.06 \text{ km})$  given in the JMA catalog [4].

#### 4.6 Real-time monitoring of CQK and CQT

The CQK and CQT are unique amplitude and phase relationships among  $A(DEP, \tau), A(INT, \tau),$  and  $A(MAG, \tau)$  at time  $\tau$ , for which a time shift to the current time  $j (= \tau + w + s)$  does not change the property of the CQK and CQT. Thus, the real-time and automatic detection of CQK and CQT is also available by monitoring the EQ particle's movement power. The power is the time-rate change of the kinetic energy defined by  $PW(c, \tau) = V(c, \tau) \times A(c, \tau)$ . For the real-time monitoring at the current time  $j = \tau + w + s$  in  $A(c, \tau)$ , the power is  $PW(c, j) = V(c, j) \times A(c, j)$ , as in section 6 [32].

#### 4.7 GPS observation of CQK and CQT processes with $PW(c, j)$

Suppose an anomaly in the crustal responses to an external force is a change comparable to or less than the amplitude fluctuations in  $\{c\}$ . In that case, it will be indistinguishable from the background trends and fluctuations. It may appear as subtle changes in their phases and magnitudes. An automated and real-time power monitoring,  $PW(c, j)$ , is a well-established and patented method to locate anomalies and prevent real-time industrial system failures and disasters [32]. Some other applications are to detect and locate such anomalies as the most critical information for bio-medical engineering [33, 34], industrial [35], and physical [36, 37] systems.

The daily displacements at a GPS station are  $\{c\}$  of Eq. (1) in a Cartesian coordinate system with  $c = E$  (west to east),  $N$  (south to north), and  $h$  (down to up) in right-handed  $(E, N, h)$ . Each displacement is noisy and non-time-differentiable; however,  $\{c\}$  has the crustal responses to the lunar tidal force loadings. Extracting a tidal force loading, for example, fortnightly (bi-weekly) loading from daily displacement series  $\{c = h\}$  under the  $\pm 20 \text{ mm}$  noise requires  $w \approx 2$  and  $s \approx 7$  to obtain  $D(c, \tau), V(c, \tau),$  and  $A(c, \tau)$ . The periodic responses to the lunar loadings expect standard unless the regional frictional failure stress state is in an imminent CQK or CQT. The  $PW(h, j)$  detects unusual crustal responses to the fortnightly tidal loading about two weeks before EQs with  $MAG \geq$  about 5 [38]. Thus, the GPS  $PW(c, j)$  monitoring of the periodic lunar tidal force loadings is a real-time supplementary tool to follow CQK or CQT.

### 5 Megathrust EQ genesis processes and predictions

#### 5.1 CQK and CQT processes

The 2011 Tohoku M9 EQ genesis processes in a Tohoku mesh  $(36^\circ\text{--}40^\circ, 138^\circ\text{--}143^\circ)$  had the CQK and CQKD established by 24 Feb 2011, 16 days before the M9 event [6]. There are neighboring meshes [6, 7, 13]; mesh  $(32.5^\circ\text{--}38^\circ, 136.5^\circ\text{--}142^\circ)$  having CQT and CQTD, and mesh  $(36^\circ\text{--}40^\circ, 136^\circ\text{--}140^\circ)$  having CQT and CQTD on the same date [6]. The

three significant EQ genesis processes suggest that they are all coupled with the M9 event on 11 Mar [6]. The Tohoku CQK shows  $A(LON, \tau a) > 0$  and  $A(LAT, \tau a) < 0$  with  $|A(LON, \tau a)| > |A(LAT, \tau a)|$ , suggesting that the horizontal force will induce share stress making the hanging wall slip to  $113^\circ (= 90^\circ + \text{about } 45^\circ / 2)$  clockwise from N. The slip direction is perpendicular to the east coastline in Fig. 3. The force  $F(c, \tau)$  with  $c = LAT, LON,$  and  $DEP$  will make the hanging wall (the Tohoku east coast) slip upward. It will generate a reverse fault as in Fig. 4c. The Tohoku M9 EQ had the focal mechanism of (Strike, Dip, Rake) =  $(193^\circ, 10^\circ, 79^\circ)$  [27]. The observed slipping direction of the hanging wall is  $114^\circ (= 193^\circ - 79^\circ)$  clockwise from N in the fault plane having a shallow dip angle of  $10^\circ$ . The rake of the dip-slip vector was almost perpendicular to the reference strike along the east coastline. Thus, the focal mechanism was in harmony with the predicted fault movement. The CQK seismogenic structure is also in harmony with the east coastline of the low Coda Q map [6, 7, 25]. As for the prediction of the focus and rupturing date made on 24 Feb 2011, they were  $(38.24^\circ, 142.82^\circ, 19 \text{ km})$  in  $(LAT, LON, DEP)$ , and in 3 events (9 Mar 2011) by  $A(DEP, tr)$  or 6 events (21 Mar 2011) by  $A(INT, tr)$  [6] in harmony with the observed focus of  $(38.10^\circ, 142.85^\circ, 24 \text{ km})$  on 11 Mar 2011. However, the Tohoku CQK and CQKD showed that the predicted fault width  $W = 17 \text{ km}$  was much less than  $W = 200 \text{ km}$  in Fig. 3 and Fig. A1 [6–8]. The mesh size for significant EQ predictions appears inappropriate for the megathrust EQ’s fault size prediction.

Another megathrust EQ was the 2003 Off-Tokachi M8 EQ in Fig. 3. The M8 EQ source parameters are; focus =  $(41.78^\circ, 144.08^\circ, 42 \text{ km})$ , origin time = 04:50 on 27 Sep 2003, and focal mechanism =  $(260^\circ, 6^\circ, 144^\circ)$  in (Strike, Dip, Rake) [27]. The Tokachi M8 had a consecutive CQK and CQT in the Hokkaido mesh  $(40.5^\circ\text{--}45.5^\circ, 141.5^\circ\text{--}145.5^\circ)$  [13]. The EQ prediction with CQT made on 31 Aug 2003 was the fault width  $W = 25 \text{ km}$  ( $M = 7.0$  with the assumption of  $L = 2W$ ), the focus of  $(42.38^\circ, 143.73^\circ, 66.57 \text{ km})$ , and the rupturing date and time of 27 Sep 2003 06:00 (8 events = 28.4 days from 31 Aug 2003) [13]. The Tokachi CQT shows  $A(LON, \tau a) > 0$ ,  $A(LAT, \tau a) < 0$ , and  $|A(LON, \tau a)| > |A(LAT, \tau a)|$ , suggesting that the horizontal force made the hanging wall (Tokachi east coast) slip to  $113^\circ (= 90^\circ + \text{about } 45^\circ / 2)$  clockwise from N in harmony with the observed rake of dip-slip vector,  $116^\circ (= 260^\circ - 144^\circ)$  clockwise from N in the fault plane at a shallow dip angle of  $6^\circ$ . However, the vertical force with  $A(DEP, \tau a) > 0$  points downward from the Earth’s surface, contradicting the rake of  $144^\circ$ . The dip-slip vector points upward  $36^\circ$  from the reversed reference strike (from the Tokachi east coast from SW to NE, as in Fig. 3). Although no Coda Q map is available for the Hokkaido area [25], the Tokachi M8 had an exceptional CQT with preceding CQK. The Tokachi M8 generated the highest tsunami of 2.25 m [39], much less than the Tohoku M9 tsunami above 9.3 m [39]. The Tohoku CQK had an upward dip-slip vector directed to  $79^\circ$  relative to the reference strike. The reference is the Tohoku east coastline from NNE to SSW, as in Fig. 3. Thus, the megathrust EQ with a consecutive CQK and CQT may account for a small angle of  $36^\circ$ -dip-slip vector to generate the 2.25 m height tsunami. The aftershock distribution shows the fault size of  $(W, L) = (160 \text{ km}, 140 \text{ km})$  [40].

## 5.2 GPS observations

Figure 3 shows the foreshocks, aftershocks, and vertical co-seismic displacements of the Tohoku M9 EQ. The GPS stations [5] in Fig. 3a and Fig. A1 had co-seismic downward and upward displacement along the east and west coast and the no-displacement along a ridge on Tohoku. The aftershock distribution and co-seismic displacements suggest that the EQ’s rectangular fault surface had a 500 km length and a 200 km width. Thus, the GPS observation suggests the correct fault length estimation is the daily displacement analyses at the GPS stations in Tohoku and the Northwest Pacific Ocean.

The  $\{c\}$  of Eq. (1) is the GPS displacements in a Cartesian coordinate system with  $c = E$  (west to east),  $N$  (south to north), and  $h$  (down to up) in right-handed  $(E, N, h)$ . Each displacement is noisy and non-time-differentiable; however,

Physical Wavelets with  $w = 200$  and  $s = 300$  in days define smooth  $D(c, \tau)$ ,  $V(c, \tau)$ , and  $A(c, \tau)$ . Then, a  $D(h, \tau) - V(h, \tau)$  path shows a resolution of 0.1 mm, four orders of magnitude greater than the daily vertical displacement noise level of  $\pm 20$  mm, and the rate change resolution of 0.01 – 0.0001 mm per day [6, 8]. The  $D(c, \tau) - V(c, \tau)$  paths describe the Tohoku M9 EQ genesis process as a bulge deformation over approximately 500 km of Tohoku shores (east and west).

As for the Northwest Pacific Ocean near the Japan Trench, there are three islands with GPS stations: Minamitorishima, Hahajima, and Chichijima, as in Figs. 3. Minamitorishima station is on the northwestern Pacific Plate. Chichijima and Hahajima stations are located below the Japan Trench and on the western edge of the Ogasawara Plateau [5]. Their qualitatively identical GPS displacement time series  $\{c\}$  suggests that Chichijima and Hahajima stations are on the western edge of the subducting northwestern Pacific Plate, and Minamitorishima station is under the northwestern Pacific Plate's motion. The GSI permanently closed Chichijima station (27.0956° N, 142.1846° E) on 9 Mar 2011. The last observation was on 8 Mar, three days before the Tohoku M9 EQ on 11 Mar 2011. Chichijima-A station (27.0675° N, 142.1950° E) started its observation on 4 Dec 2007, and replaced the Chichijima station.



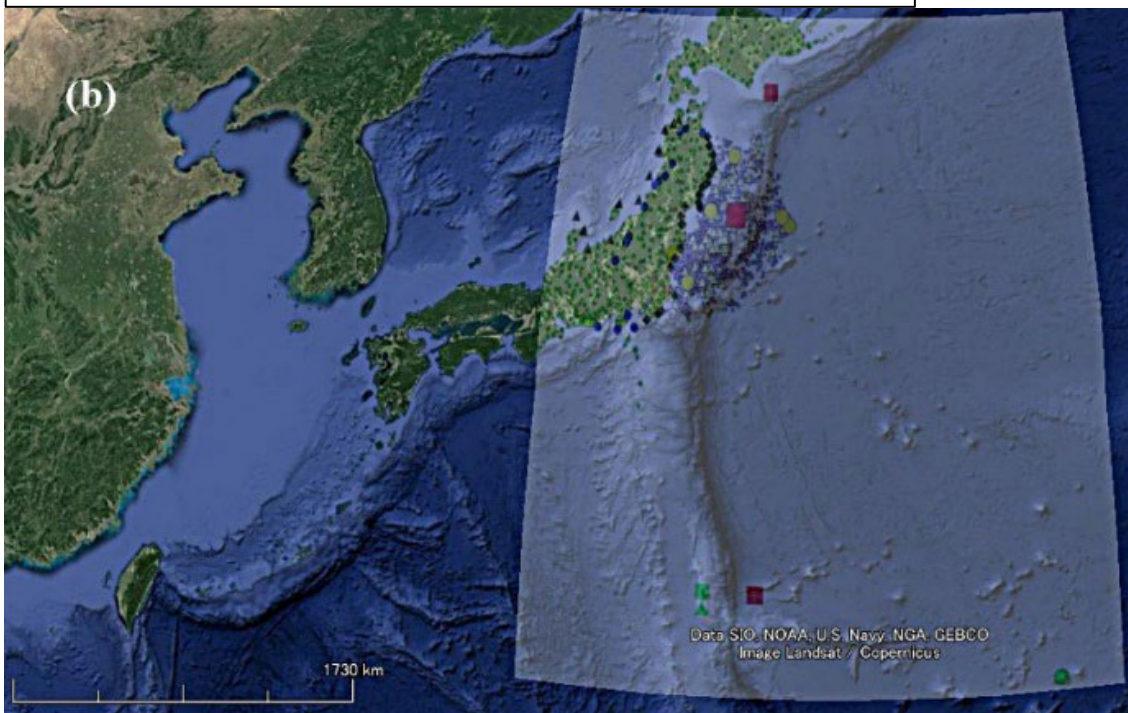
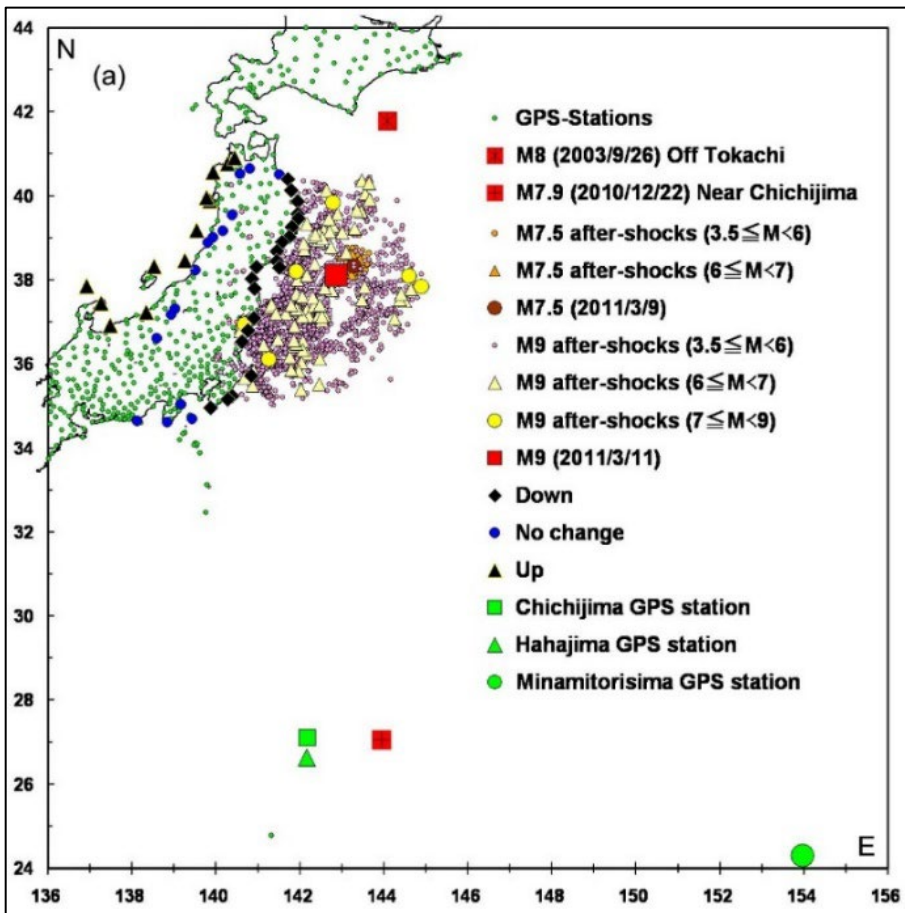


**Figure 3. GPS stations, vertical co-seismic displacement, foreshocks, and aftershocks of the M9 EQ**

Modified and reproduced from [6–8]. Magnified graphs and a map are in Appendix. (a) The EQ source parameters are from the JMA’s unified focus catalogs [4]. The EQ magnitude  $M$  is JMA’s magnitude. The off Tokachi M8 (2003/9/23) EQ [11] was the megathrust EQ in section 5.1. The M7.5 (2011/3/9) EQ is a foreshock of the Tohoku M9 EQ (2011/3/11). The M9 had the focus of ( $38.1006^\circ\text{N}$ ,  $142.8517^\circ\text{E}$ , 24 km), and the reverse faulting of (Strike, Dip, Rake) = ( $193^\circ$ ,  $10^\circ$ ,  $79^\circ$ ) [27]. The vertical co-seismic displacements over the 500 km distance are downward (Down), upward (Up), and no change (No change) displacement at each GPS station. Three GPS stations above 38 degrees north latitude-line, used for Fig. 4, are Ryoutsu2 (Up) at ( $38.0633^\circ\text{N}$ ,  $138.4717^\circ\text{E}$ ,



west coast), Murakami (No change) at (38.2307° N, 139.5069° E), and Onagawa (Down) at (38.4492° N, 141.4412° E, east coast). Their observations show the Tohoku bulge deformation processes as in Figs. 4 and 5. The M9 EQ (2011/3/11) is on the 38-degree N line. The GPS stations in the Northwest Pacific Ocean are Chichijima, Hahajima, and Minamitorishima. Chichijima and Hahajima stations are on the subducting western edge of the northwestern Pacific Plate, whereas Minamitorishima station is on the northwestern Pacific Plate (far right below). The Chichijima, Hahajima, and Minamitorishima stations observed the identical abnormal oceanic plate motion coupled with the bulge deformation along the Tohoku east coast. As in Fig. 6, the Pacific Plate's abnormal westward motion triggered the M7.9 (2010/12/22) EQ of the normal faulting in the plate slab near Chichijima. The EQ had the focal mechanism of (Strike, Dip, Rake) = (109°, 46°, -131°) [27]. The hanging wall slipped to 240° clockwise from N, along the plate's westward motion. (b) A google earth map with Fig.3a overlaid.

### 5.3 Bulge deformation

The Tohoku GPS stations observed a bulge deformation, as shown in Fig. 4 [6, 8]. A regular deformation by the tectonic plate-driving forces is the schematic of Fig. 4a. It had an upward rate of 1.5 mm per year on the west coast and a subsidence rate of 6 mm per year on the east coast. The westward movement of the subducting northwestern Pacific Plate was 0.1 mm per day over ten years. The plate had northward movement at an average rate of 0.03 mm per day. The 0.1 mm per day is approximately our fingernail's growth rate.

An upheaval of 1 – 3 mm grew in three phases. They are initial S0, transitional S1, and final S2 in the  $D(h, \tau) - V(h, \tau)$  path of Fig. 5b. Only the equations of motion and a smooth  $D(h, \tau) - V(h, \tau)$  path with the parameters like  $w = 200$  and  $s = 300$  in days can quantify the three-phase deformation.

In Jan 2010, the initial phase began a uniform upward increase of  $A(h, \tau)$  out of the regular deformation, as in Fig. 5b. Preceding the initial, on 23 Nov 2009, the west coast (W) started to slow down the eastward movement. During the initial phase in Fig. 4a, the east coast (E) subsided by 2.8 mm over 149 days, as in segment S0. The west coast (W) and the Top followed the east coast with 1 mm and 1.5 mm subsidence. Their subsidence was unexpected, suggesting an action to make the overriding tectonic plate's eastern edge take hold of a significant barrier (fault) 2.8 mm deep. The east coast edge went further down by 3.3 mm to begin pulling the subducting oceanic plate with a lifting (bulging) force on the fault surface, which is segment S1 of the  $D(h, \tau) - V(h, \tau)$  path. The action on the east and west coasts started on 9 and 7 Jun 2010. As shown in Fig. 4b, Tohoku's east coast began to pull the subducting plate by the fault coupling on 11 Jul 2010, nine months before the Tohoku M9 EQ. Figure 6b shows the pulling accelerated the oceanic plate's westward motion to reach an abnormal speed of 0.69 mm/day by 22 Dec 2010, approximately three times higher than 11 Jul 2010.

On 14 Nov 2010, before the highest speed observation, the bulge deformation began the final phase S2 with an upheaval growing along the east coast. By 10 Mar 2011 (one day before the Tohoku M9 event), the upheaval grew to 1.2 mm over 115 days from 14 Nov 2010 [8]. Similarly, an upheaval of 2.3 mm on the west coast began on 29 Oct 2010, and 2.5 mm on the Top began on 26 Aug 2010 [8].

During the three-phase bulge deformation, the force  $A(E, \tau)$  of the overriding tectonic and the subducting oceanic plate compressed Tohoku, centered at the ridge (Top), westward by 13.2 mm and eastward by 18.4 mm [8]. The Top moved westward by 1.2 mm. The west coast began the push 173 days earlier than the east coast, suggesting the overriding tectonic plate exerted an enormous eastward push on the west coast. The initial bulge phase was the push on the regular deformation of Fig. 4a. Figure 4b shows the bulge transition and final phase, whose timeline is in harmony with a pre-seismic microgravity anomaly observed by the GRACE satellite data from Jul 2010 to Feb 2011 [41]. The upheaval

timeline near the Tohoku M9 epicenter area is in harmony with an uplift suggested by the sea-surface gravity change observation [42].

As the upheaval grew, the oceanic plate's westward motion decelerated and stopped by 21 Feb 2011. In four days, the motion reversed direction. The  $D(E, \tau) - V(E, \tau)$  path in Fig. 6c shows the eastward speed reaching 0.06 mm/day by 8 Mar 2011. Linear upheaval generated and released an enormous reaction force, as in Fig. 4c. The three-phase bulge deformation, which pulled the subducting oceanic plate, is the GPS observed Tohoku M9 EQ genesis process over 15 months. So-called slow-slip events were not in the process [8].

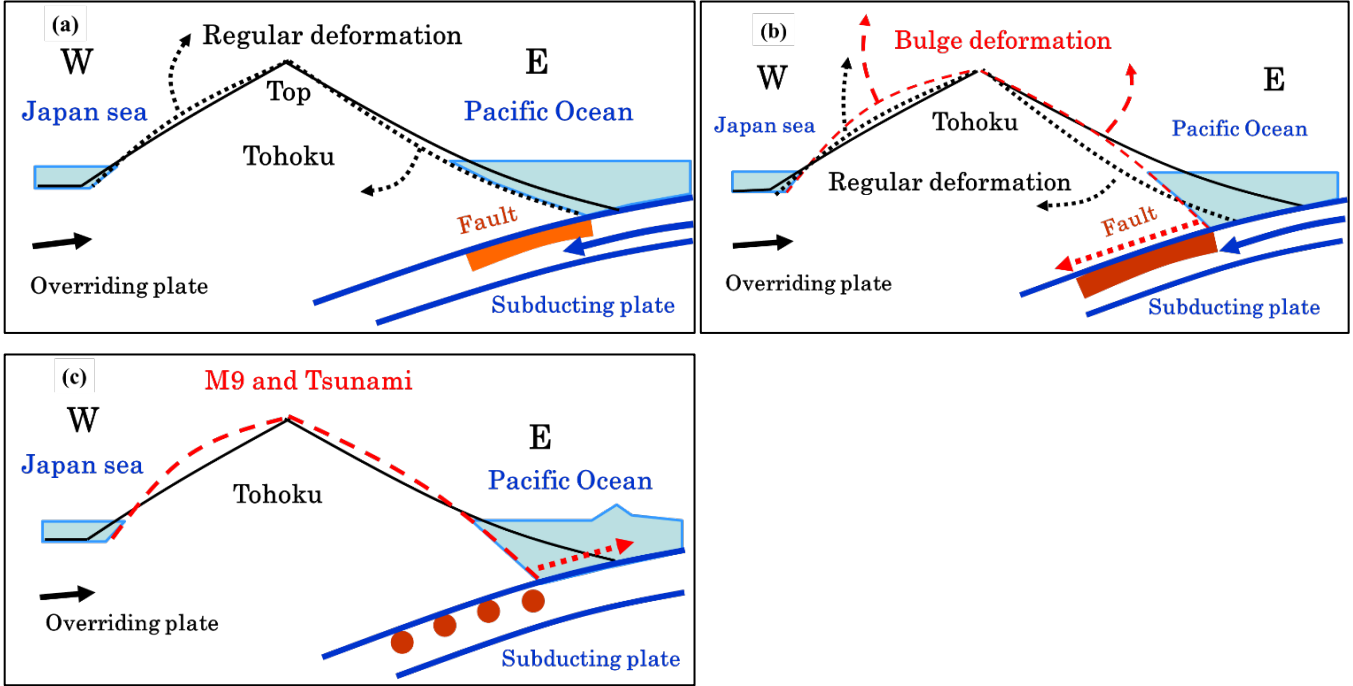


**Figure 4. Three phases of crustal deformation (a megathrust EQ genesis process)**

Modified and reproduced from references [6, 8]. The E, W, and Top are for the East coast (Onagawa station), West coast (Ryoutsu2 station), and Top (Murakami station). (a) A regular slow deformation had the initial bulge phase characterized by a uniformly increasing acceleration  $A(h, \tau) (> 0, \text{upward})$ . (b) The transition is from the regular to a bulge deformation, which pulled (dotted arrow) the subducting Pacific Plate by coupling with the fault. (c) The final phase is the upheaval deformation activating an enormous reaction (dotted arrow) to rupture the megathrust EQ and a tsunami.

The  $D(h, \tau)$  and the  $D(h, \tau) - V(h, \tau)$  path in Figs. 5a and 5b show an upheaval of 1.2 mm over 115 days began at dot-arrows, 'Bulge starts' indicating the onset of the final phase. The onset time is  $\tau = 3615$ , 29 Nov 2009, 350 days behind 14 Nov 2010, in real-time  $j$ . The date precedes 22 Dec 2010, when the westward speed of the subducting northwestern Pacific Plate became abnormal, as in Fig.6.

The  $D(h, \tau) - V(h, \tau)$  path in Fig. 5b shows three approximately linear segments; the initial bulge phase (S0) with a nearly zero slope, the transitional phase (S1) with a minus slope in subsidence, and the final phase (S2) with a positive slope in upheaval. All segments are under positive  $A(h, \tau)$  that grew linearly in time  $\tau$ , suggesting the bulge deformation on the east coast GPS station was under a lifting force.

Segment S1 of the  $D(h, \tau) - V(h, \tau)$  path has  $\Delta D(h, \tau) = -3.3\text{mm}$  (subsidence) and  $\Delta V(h, \tau) = +0.0142\text{ mm/day}$  over 158 days in time  $\tau$ . It is from  $\tau = 3457$  on 24 Jun 2009 to  $\tau = 3615$  on 29 Nov 2009, and from  $j = 3807$  on 9 Jun 2010

to  $j = 3965$  on 14 Nov 2010, in real-time  $j$ . The average acceleration was  $+ 8.99 \times 10^{-5}$  mm/day<sup>2</sup>, exerting the upward acceleration (Force) on the east coast GPS station.

Segment S2 has  $\Delta D(h, \tau) = 1.2$  mm (upheaval) and  $\Delta V(h, \tau) = + 0.0054$  mm/day over 115 days from  $j = 3965$  on 14 Nov 2010 to  $j = 4080$  on 10 Mar 2011, one day before the M9 event. The average acceleration is  $+ 4.7 \times 10^{-5}$  mm/day<sup>2</sup>.

The  $D(h, \tau) - V(h, \tau)$  paths in Fig. 5 show an approximately constant downward speed of  $V(h, \tau) \approx - 0.018$  mm/day (Fig. 5b) with  $w = 200$  and  $s = 300$  except for a significant co-seismic downward displacement. No appreciable change in  $V(h, \tau)$  suggests  $A(h, \tau) \approx 0$ . The  $A(h, \tau)$  in Fig. 5b shows a slight fluctuation until it begins a steady increase at S0. Thus, the regular subsidence deformation at the east coast in Fig. 4a had no significant vertical force component.

Figures 5b and 5c show the positive acceleration (lifting force) in segments S0, S1, and S2, suggesting that they are part of a bulge deformation under the negatively (westwardly) increasing  $V(E, \tau)$  and  $A(E, \tau)$ . Thus, the well-known elastic-rebound theory cannot explain the sudden appearance of the upward force component ( $A(h, \tau) > 0$ ) nearly normal to the fault line (surface) shown in Fig.4b.

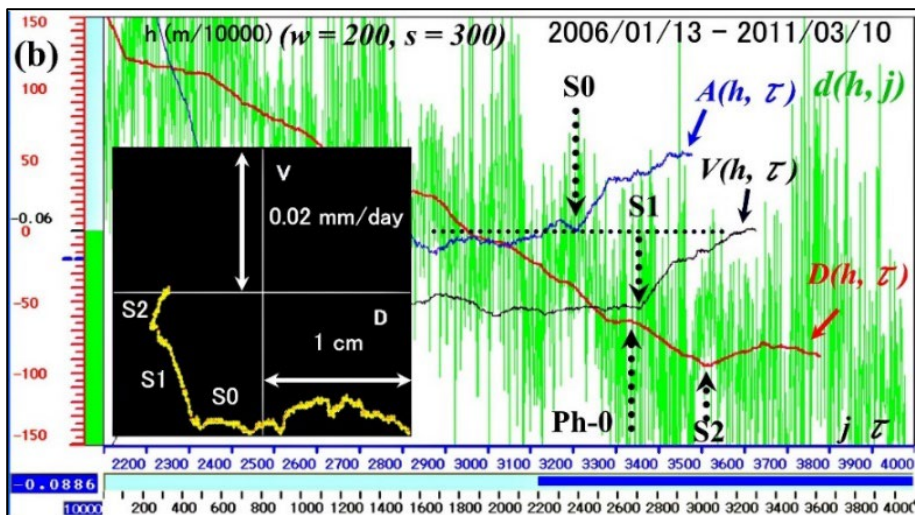
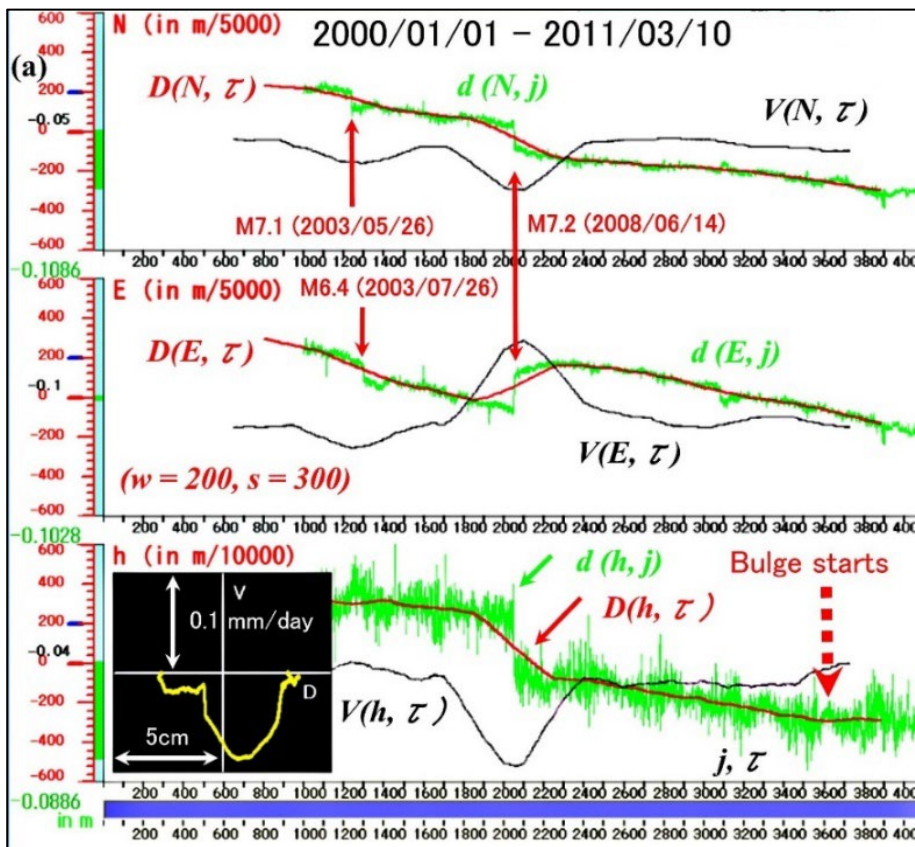
The downward (westward) bend on the  $D(E, \tau) - V(E, \tau)$  path in Fig. 5c started at  $\tau = 3434$  on 1 Jun 2009, which is 17 May 2010, in real-time  $j = \tau + 350$ . The westward bend-onset denoted by Ph-0 preceded S1-onset by 23 days. The westward movement from Ph-0 was  $D(E, \tau) = - 13.2$  mm by 10 Mar 2010, one day before the Tohoku M9 event.

The  $D(h, \tau) - V(h, \tau)$  path's S1 is part of the bulge deformation process at Onagawa station. However, we refer to the transition from S1 to S2 as the bulge deformation onset (bulge-onset) or 'Bulge starts' for the automated detection by real-time power monitoring in section 6.

Segment S1 has a lifting force twice stronger as the S2 force. The S1-onset was at time  $\tau = 3457$  (on 14 Jun 2009), including  $d(h, j)$  at time  $j = 3807$  (on 9 Jun 2010). The date precedes 11 Jul 2010, when the westward motion's trend change began. The S1 ends at the bulge-onset,  $\tau = 3615$ , 29 Nov 2009 350 days behind 14 Nov 2010, in real-time  $j$ . The date precedes 22 Dec 2010, when the abnormal westward speed of the subducting Pacific Plate became about three times higher than the standard speed. Thus, the bulge deformation is the geophysical origin of the abnormal westward motion of the subducting oceanic plate.

We note that each linearity of S1 and S2 holds for the respective  $D(h, \tau) - A(h, \tau)$  path. However,  $A(h, \tau)$  at the S2-onset ( $\tau = 3615$ ) requires  $d(h, j)$  at  $j = 4115$  ( $> j = 4080$ , 10 Mar 2011). Thus, the second linear segment is not available.

As in Figs. 6d and 6g, the observation in low-frequency selection accompanies some onset-detection delay in real-time  $j$ . However, the equations with  $w \approx 200$  and  $s \approx 300$ , even with a much longer real-time delay, are requisite for quantifying the Tohoku's crustal-bulge deformation in a three-phase process by minimizing the yearly and seasonal variations and environmental noises in  $\{c\}$  ( $c = h$ ).





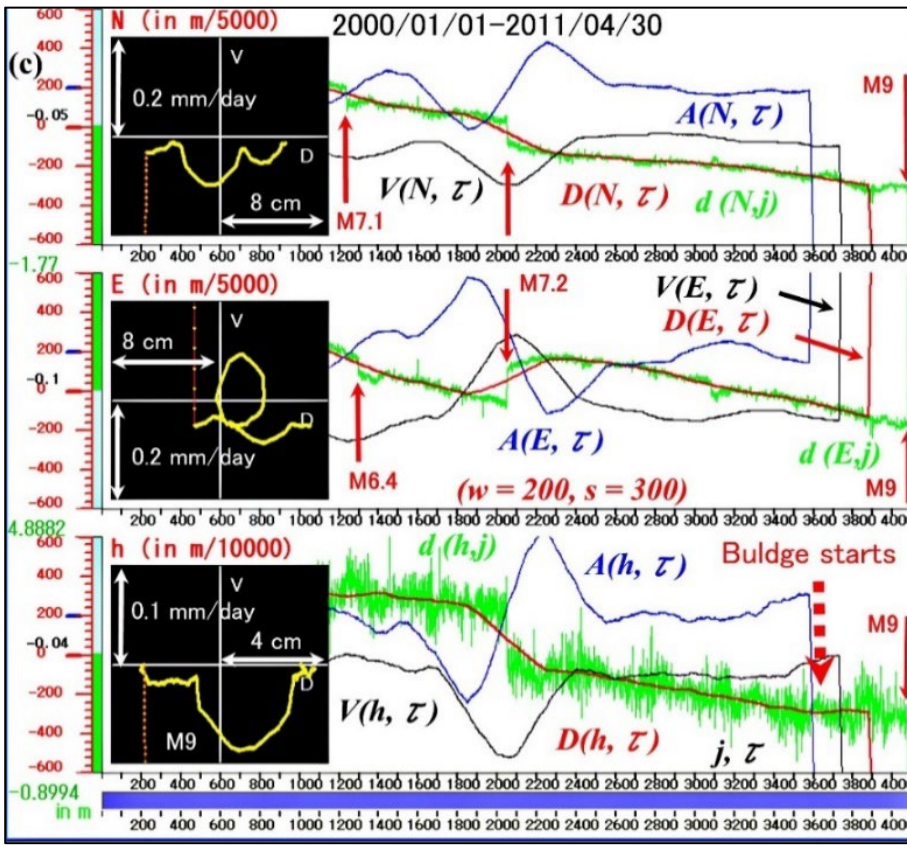


**Figure 5. The bulge and M9 observations at Onagawa station (east coast)**

Modified and reproduced from references [6, 8]. (a) The original  $\{c\}$  is from 1 Jan 2000 ( $j = 0$ ) to 10 Mar 2011 ( $j = 4080$ ). Sudden large shifts in  $\{c\}$  are co-seismic. The events' magnitudes and dates in (yyyy/mm/dd) are at arrows on  $d(c, j)$ . The  $w = 200$  and  $s = 300$  are for  $D(c, \tau)$ ,  $V(c, \tau)$ , and  $A(c, \tau)$ . The  $D(h, \tau) - V(h, \tau)$  plane is (5 cm, 0.1 mm/day) with the offset origin  $D(h, \tau) = -0.04$  m and  $V(h, \tau) = 0$  mm/day. The bulge-onset is at arrow 'Bulge starts' on the  $D(h, \tau)$  at  $\tau = 3615$ , 29 Nov 2009 (14 Nov 2010, in real-time  $j$ ).

(b) The expanded window is from 13 Jan 2006 to 10 Mar 2011. The magnified phase-plane is (1 cm, 0.02 mm/day) with the origin  $D(h, \tau) = -0.062$  m ( $-0.06$  m  $-0.002$  m). Approximately linear segments are S0, S1, and S2 on the phase plane. Each segment's onset location is at a dotted arrow with its name. The S2 is the 'Bulge starts' in Fig. part a. Arrow Ph-0 between S0 and S1 is the onset location of an abnormal movement on the  $D(E, \tau) - V(E, \tau)$  path in Fig. part c. A horizontal dot-line at the offset origin 0 ( $-0.06$ ) is the abscissa for  $V(h, \tau)$  and  $A(h, \tau)$ ; namely,  $V(h, \tau) = A(h, \tau) = 0$ . The magnitudes of  $V(h, \tau)$  and  $A(h, \tau)$  are on relative scales.

(c) The original  $\{c\}$  is from 1 Jan 2000 ( $j = 0$ ) to 30 Apr 2011 ( $j = 4107$ ). It includes the M9 event on 11 Mar 2011 ( $j = 4081$ ) and arrow M9 on  $d(c, j)$ . The  $D(c, \tau) - V(c, \tau)$  planes with the offset origins are (8 cm, 0.2 mm/day) for  $c = N$  and  $E$ , and (4 cm, 0.1 mm/day) for  $c = h$ . The  $D(c, \tau) - V(c, \tau)$  path shows the dotted path jumped by the M9 event. Every  $d(c, j)$  and its column height has the co-seismic shifts saturated by the M9 event with its digital value from the position at  $j = 0$ . The southward shift is 1.90 m ( $-1.77 - 0.05 - 0.08$ ), the eastward shift is 4.7482 m ( $4.8882 - 0.10 - 0.04$ ), and the downward shift is 0.9694 m ( $= -0.8994 - 0.04 - 0.03$ ).

#### 5.4 Abnormal movements of the oceanic plate and real-time monitoring

The bulge deformation of the overriding Tohoku crust pulled the subducting northwestern Pacific Plate. The displacement  $\{c\}$  of the oceanic plate motion is under the lunar synodic tidal force loading. Thus, monitoring the plate responses to the periodic lunar tidal force loadings is a tool to detect subtle changes and abnormal movements in pulling. The oceanic plate has three islands with GPS stations, as in Fig. 3.

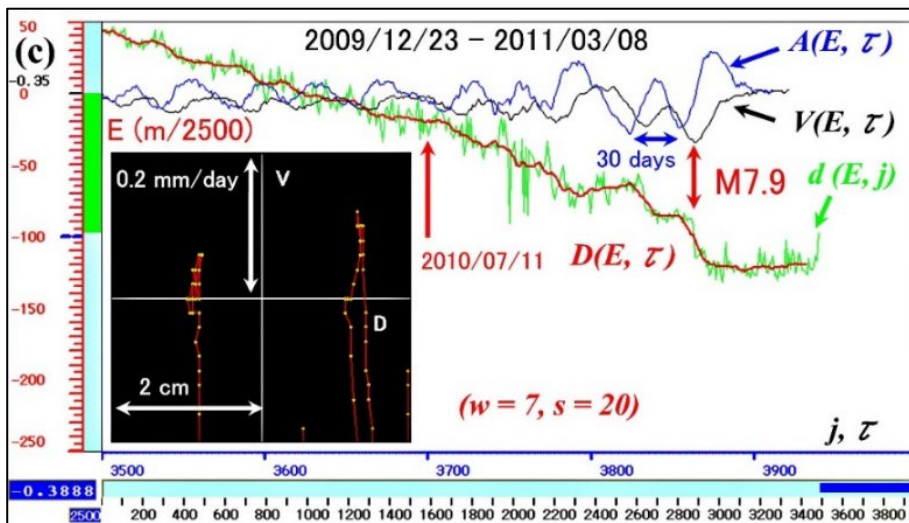
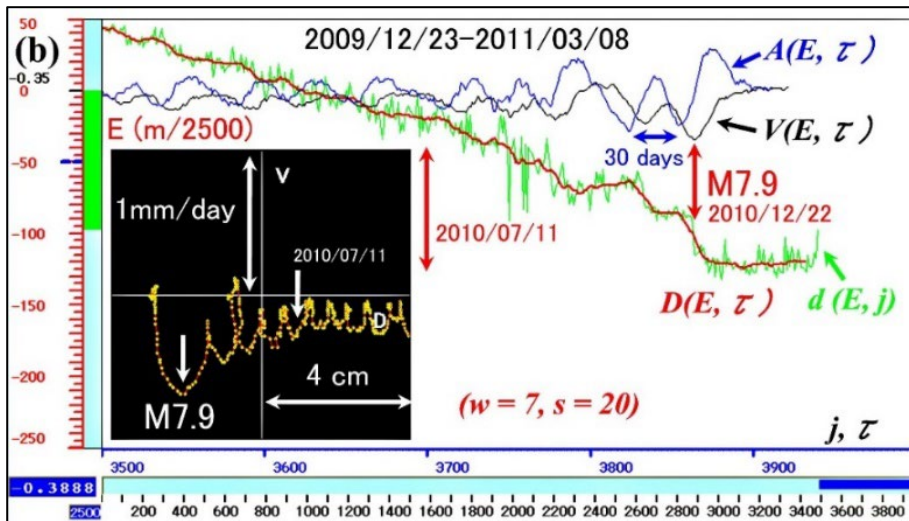
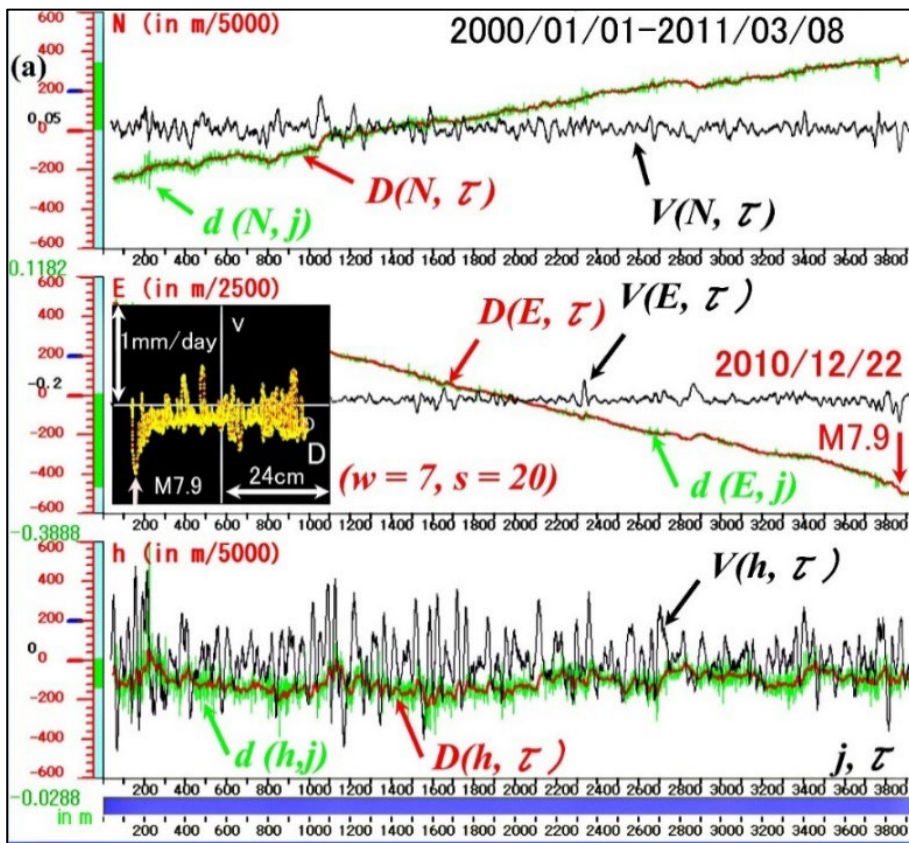
We define the  $D(c, \tau)$ ,  $V(c, \tau)$ , and  $A(c, \tau)$  with  $w = 7$  and  $s = 20$  to observe the responses of the oceanic plate motion to the synodic loading of period 30 (29.5) days. Any external force coupling with the overriding eastern edge may change the periodic lunar responses in amplitudes and phases.

As in Fig. 6 of Chichijima station, an unexpectedly increased westward speed appeared on the  $D(E, \tau) - V(E, \tau)$  path. A trend-change on  $D(E, \tau)$  in Jul 2010 preceded the abnormal motion. The westward speed  $V(E, \tau)$  reached its highest on 22 Dec 2010, 76 days before the Tohoku M9 EQ. It was  $-0.69$  mm/day, approximately three times higher than the standard westward speeds. A rapid deceleration followed, stopping the westward motion around 21 Feb 2011. In about four days, the moving direction reversed, and the subducting plate moved eastward until the Tohoku M9 events on 11 Mar 2011. Other GPS island stations in the Northwest Pacific Ocean observed the same abnormal movements as in Table 1 [8].

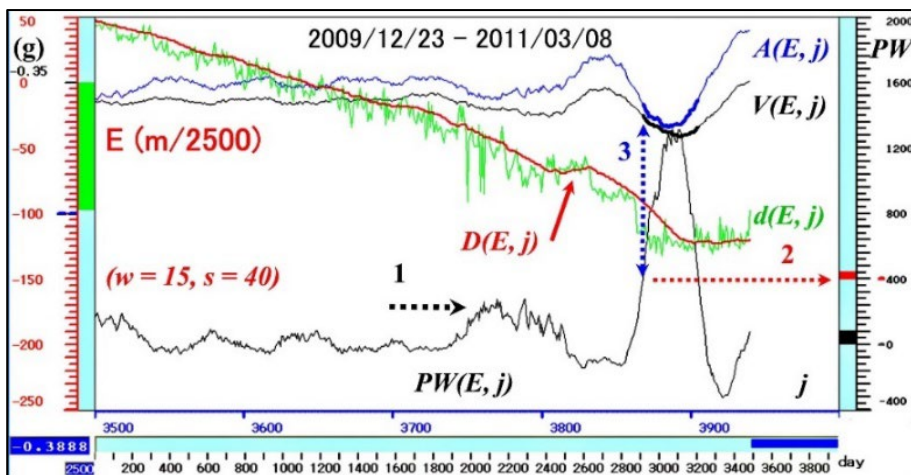
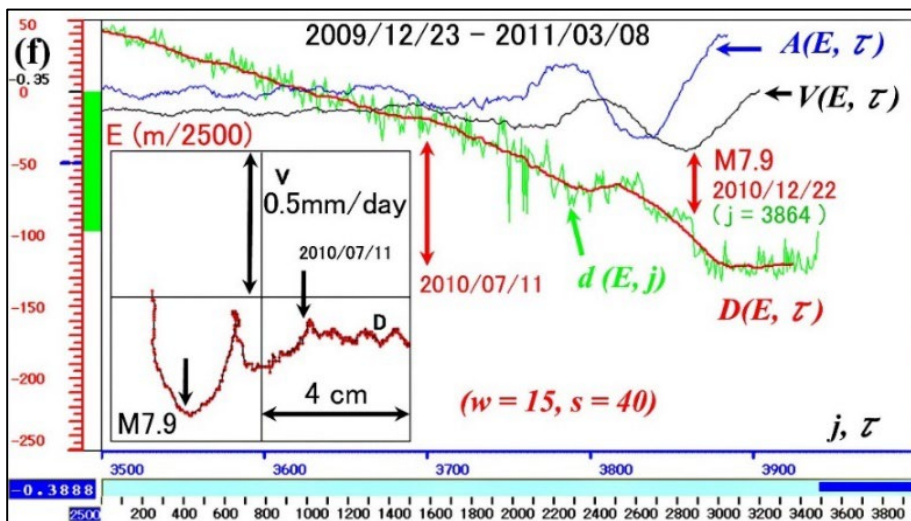
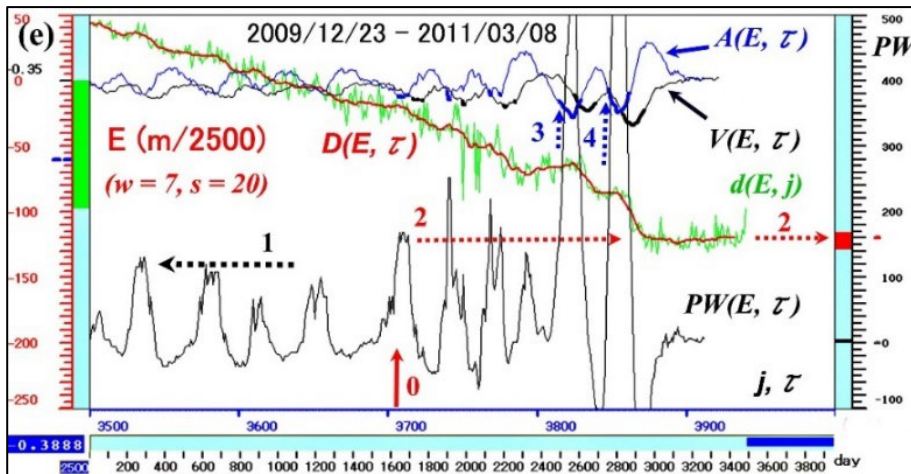
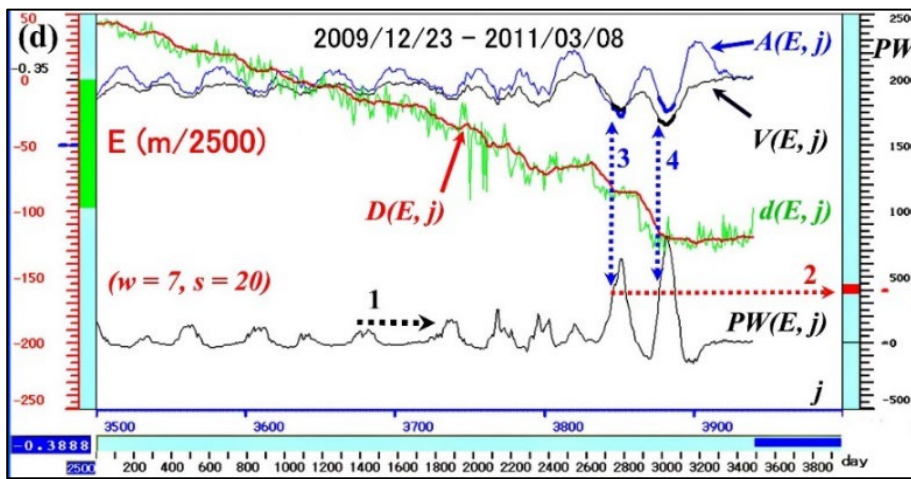
**Table 1 (Abnormal motion of the subducting northwestern Pacific Plate)**

Westward(-) and Eastward(+) speed $V(E, \tau)$ mm/day								
GPS station	$D(E, \tau)$ trend change		Max $V(E, \tau)$		$V(E, \tau)$ and $D(E, \tau)$ mm on March 8 and 10			
	yyyy/mm/dd	$V(E, \tau)$	yyyy/mm/dd	$V(E, \tau)$	March 8		March 10	
Chichijima	2010/07/11	-0.25	2010/12/22	-0.69	+0.06	+1.6 mm		
	No observation after 2011/03/08							
Chichijima-A	2010/07/11	-0.26	2010/12/22	-0.78	+0.08	+2.0 mm	+0.12	+2.4 mm
Hahajima	2010/07/11	-0.28	2010/12/22	-0.84	+0.12	+2.0 mm	+0.20	+2.5 mm
Minamitorishima	2010/07/11	-0.34	2010/10/08	-1.15	0.00	0.0 mm	+0.05	0.0 mm
	No data available; 2010/08/07~2010/09/25, 2010/10/13~2011/01/01							

As in Figs. 6d and 6e, the power monitoring in section 6 detected the onset for both the trend-change and the abnormal motion. We can remove the lunar synodic loading with  $w = 15$  and  $s = 40$ , as in Fig. 6f. The  $PW(E, j)$  monitoring detected the anomaly onset more clearly, as in Figs. 6g and 6h. The unexpected trend-change on  $D(E, \tau)$  was in Jul 2010 in Fig. 6h, which was the first response of the subducting oceanic plate to the overriding eastern edge's bulge formation.









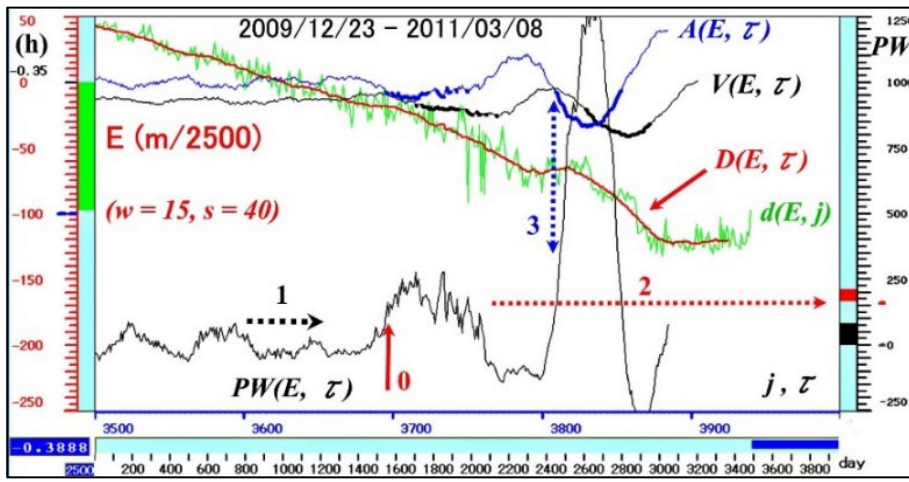


**Figure 6. The abnormal westward motion at Chichijima station**

Modified and reproduced from references [6, 8]. (a) The original  $\{c\}$  is from  $j = 0$  (1 Jan 2000) to  $j = 3940$  (8 Mar 2011). Parameters  $w = 7$  and  $s = 20$  are for  $D(c, \tau)$ ,  $V(c, \tau)$ , and  $A(c, \tau)$ . The  $D(E, \tau) - V(E, \tau)$  plane is (24 cm, 1 mm/day). Its origin is  $D(E, \tau) = -0.2$  m, the offset reference ( $-0.2$  m) at scale 0 from the first-day position ( $j = 0$ ). The  $V(E, \tau)$  origin is 0 mm/day. The right half of the  $D(E, \tau) - V(E, \tau)$  plane is east of the offset origin. The upper half is eastward and positive  $V(E, \tau)$ . The lower half is westward and negative. The M7.9 (2010/12/22) event is on  $D(E, \tau)$  at  $\tau = 3864$  and the (24 cm, 1 mm/day) path. The  $d(c, j)$  is in green,  $D(c, \tau)$  in red, and  $V(c, \tau)$  in black. The  $V(c, \tau)$  is in a relative scale from the graphical origin 0. (b) The expanded time window is from  $j = 3500$  (23 Dec 2009) to  $j = 3940$  (8 Mar 2011). The (4 cm, 1 mm/day) plane has an offset origin at the blue-line-scale  $-50$ ,  $D(E, \tau) = -0.22$  m ( $-0.2 - 50/2500$ ). The  $V(E, \tau)$  and  $A(E, \tau)$  are in relative scales from the same graphical origin, 0. The lunar synodic tidal force loading of the 29.5-day-period has 30 days on the blue  $A(E, \tau)$ . The date label 2010/07/11 is the  $D(E, \tau)$  trend change at  $\tau = 3700$  (11 Jul 2010). (c) The window is from  $j = 3500$  (23 Dec 2009) to  $j = 3940$  (8 Mar 2011). A magnified (2 cm, 0.2 mm/day) plane has the offset origin at the blue-line-scale  $-100$ ,  $D(E, \tau) = -0.39$  m ( $-0.35$  m  $- 100 \times$  m/2500). The path ended at  $V(E, \tau) = +0.06$  mm/day. (d) The window is from  $j = 3500$  (23 Dec 2009) to  $j = 3940$  (8 Mar 2011) with a  $PW(E, j)$  monitoring. The relative power scales are on the right column. The monitoring with  $PW(E, j) \geq 400$  detected an anomalous lunar synodic loading on  $\{E\}$ . The predetermined 400 was about twice the expected standard power level at arrow 1. Level 400 is at the red scale at arrow 2. Arrow 3 was the first anomaly detection at  $j = 3847$  (5 Dec 2010). At the detection,  $PW(E, j)$  rose from 378 (at  $j = 3846$ ) to 440 (at  $j = 3847$ ), showing the red column height. Arrow 4 was the second detection at  $j = 3877$  (4 Jan 2011). The anomalous  $V(E, j)$  and  $A(E, j)$  were bold under  $PW(E, j) \geq 400$ . (e) The window is from  $j = 3500$  (23 Dec 2009) to  $j = 3940$  (8 Mar 2011).  $PW(E, j) \geq 160$  found the westward trend-change at real-time  $j = 3735$  on 15 Aug 2010. In time  $\tau$ , the change was at  $\tau = 3708$  (at arrow 0) on 19 Jul 2010. The detecting level 160 at arrow 2 adopted the standard power level at arrow 1. By shifting real-time  $j$  back to time  $\tau$ , the displays are  $D(E, \tau)$ ,  $V(E, \tau)$ ,  $A(E, \tau)$ , and  $PW(E, \tau)$ . (f) The time window is from  $j = 3500$  (23 Dec 2009) to  $j = 3940$  (8 Mar 2011). Parameters  $w = 15$  and  $s = 40$  removed the 30-day-period oscillation. The (4 cm, 0.5 mm/day) plane has the offset-origin,  $D(E, \tau) = -0.37$  m ( $-0.35 - 0.02$ ) at the blue-line scale  $-50$ . The  $D(E, \tau)$  trend-change has the date label 2010/7/11. (g) The window is from  $j = 3500$  (23 Dec 2009) to  $j = 3940$  (8 Mar 2011) with  $w = 15$  and  $s = 40$ . Arrow 3 was the anomaly detection at  $j = 3869$  (27 Dec 2010) by  $PW(E, j) \geq 400$ . The threshold 400 is at the red scale pointed out by arrow 2. The threshold adopted the standard power level at arrow 1. The power column height change in red is from 400 (at  $j = 3868$ ) to 442 (at  $j = 3869$ ) at the anomaly detection. The black column height shows the last  $PW(E, j)$  (just above level 0) on 8 Mar 2011 ( $j = 3940$ ). (h) The window is from  $j = 3500$  (23 Dec 2009) to  $j = 3940$  (8 Mar 2011) for the  $D(E, \tau)$  trend-change detection. Up-arrow 0 was the trend-change detection at real-time  $j = 3751$  (31 Aug 2010) by  $PW(E, j) \geq 160$  with  $w = 15$  and  $s = 40$ . In time  $\tau$ , the change is at arrow 0,  $\tau = 3696$  on 7 Jul 2010. Arrow 1 is the standard power level, for which the unexpected level 160 was about twice the standard level.

As in Fig. 6a, series  $\{E\}$  in the second window shows the  $D(E, \tau)$  and  $V(E, \tau)$  relation expressed as a path on the (24 cm, 1 mm/day) plane. At the highest westward (downward) speed, the M7.9 EQ ruptured in the Pacific about 187 km away from the station (Fig. 3). The event had normal faulting (Strike, Dip, Rake) = (340°, 57°, -56°) [24], suggesting the abnormal westward motion triggered the event.

In Fig. 6b, the  $D(E, \tau)$ ,  $V(E, \tau)$ , and  $A(E, \tau)$  show the lunar synodic tidal force loading (the 29.5-day-period) on the subducting Pacific Plate (Chichijima station). The path moves eastward, protruding by the amount of 0.2 mm/day from the westward speed at -0.23 mm/day. Dividing the 6 mm separation between the two protruding peaks by 30 days, the westward speed estimation is -0.2 mm/day. The westward trend of  $D(E, \tau)$  changed at around  $\tau = 3700$  (11 Jul 2010), whose change has the arrowed label 2010/07/11 on the  $D(E, \tau)$ . The trend-change onset was in an insufficient synodic tidal loading on the  $D(E, \tau)$ ,  $V(E, \tau)$ , and  $A(E, \tau)$  segments that are roughly linear. The onset divided the  $D(E, \tau) - V(E, \tau)$  path into two small linear segments. The first linear segment preceding the trend-change has an explicit segment equation  $A(E, \tau) \approx K \times D(E, \tau)$ , as in the  $D(E, \tau) - A(E, \tau)$  path segment of Fig. 7. The constant  $K$  is positive. However,  $K$  is negative under effective lunar synodic tidal loading, obeying the oscillatory motion. Following the trend-change, the motion became anomalous and reached the highest westward speed of  $V(E, \tau) = -0.69$  mm/day at  $\tau = 3864$  on 22 Dec 2010, approximately three times faster than  $V(E, \tau) = -0.25$  mm/day at  $\tau = 3700$  on 11 Jul 2010. After this, the westward motion showed a rapid deceleration until it stopped at  $\tau = 3908$  on 4 Feb 2011.

Figure 6c shows a magnified path, changing  $V(E, \tau)$  positive on 8 Feb 2011. The reversed motion reached the eastward speed of  $V(E, \tau) = +0.06$  mm/day and the eastward displacement of 1.6 mm at time  $\tau = 3918$  on 14 Feb 2011. In real-time  $j$ , it was 8 Mar 2011, three days before the 11 Mar M9 EQ, because  $j$  is in advance of  $\tau$  by 17 days ( $\tau = j - s/2 - w$ ).

Figure 6d shows the  $PW(E, j) \geq 400$  monitoring detected the anomaly by a predetermined threshold level of 400. Level 400 is an unexpected power level twice the standard  $PW(E, j)$  amplitudes at dot-arrow 1. The threshold adoption can be automatic or manual during power monitoring. Arrow 3 and Arrow 4 were the first at  $j = 3847$  (5 Dec 2010) and second at  $j = 3877$  (4 Jan 2011) anomaly detections, respectively. At each detection,  $V(E, j)$  and  $A(E, j)$  become bold, and they stay bold while  $PW(E, j) \geq 400$ . They are negative, indicating the anomalous acceleration and movement were westward.

Figure 6e shows that the unexpected westward motion started at the upward arrow 0. The  $PW(E, j) \geq 160$  monitoring found the westward trend-change at real-time  $j = 3735$  on 15 Aug 2010. In time  $\tau$  ( $\tau = j - s - w$ ), it was 3708 on 19 Jul 2010. We shifted real-time  $j$  back to time  $\tau$  to draw  $D(E, \tau)$ ,  $V(E, \tau)$ ,  $A(E, \tau)$ , and  $PW(E, \tau)$ , satisfying the position and derivatives' time reversal properties. As for anomalies 3 and 4, the negative  $A(E, \tau)$  precedes negative  $V(E, \tau)$  so that the anomalous acceleration (oceanic tectonic driving force) and the motion to follow are westward.

In Fig. 6f, we define the  $D(E, \tau)$ ,  $V(E, \tau)$ , and  $A(E, \tau)$  with  $w = 15$  and  $s = 40$ , which masked the lunar synodic loading. The  $D(E, \tau) - V(E, \tau)$  path shows the abnormal  $V(E, \tau)$  more apparent than that in Fig. 6d.

Figure 6g shows that the  $PW(E, j) \geq 400$  monitoring with  $w = 15$  and  $s = 40$  detected the abnormal motion at arrow 3 (at  $j = 3869$  on 27 Dec 2010). The power change is the red column height. The  $V(E, j)$  and  $A(E, j)$  in bold are negative so that the abnormal motion was by the westward  $A(E, j)$ .

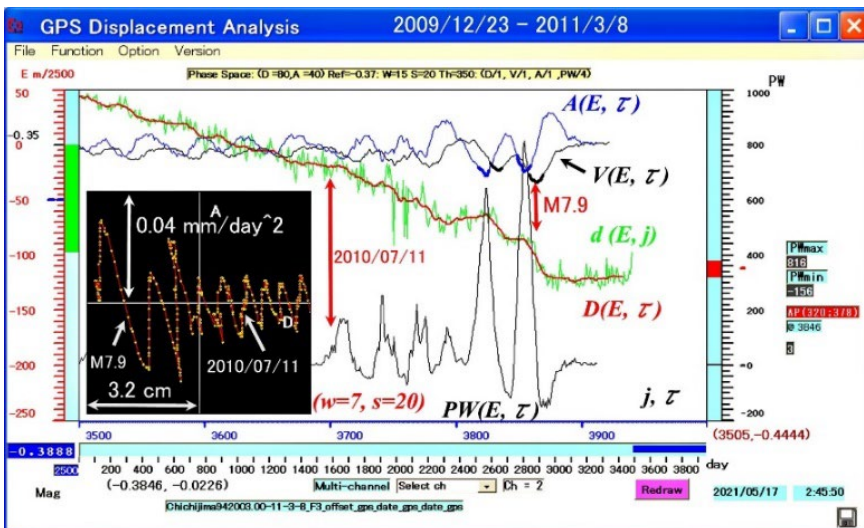
Figure 6h shows the  $PW(E, \tau) \geq 160$  monitoring with  $w = 15$  and  $s = 40$  detecting the westward trend change without the effective synodic tidal force loading on  $D(E, \tau)$ . The trend change is independent of the lunar tidal force loading. The geophysical origin for the trend-change was a transition from the regular subsidence deformation on the east coast of

Tohoku to the bulge formation, as in section 5.3. The abnormal westward motion of the subducting northwestern Pacific Plate followed the trend change.

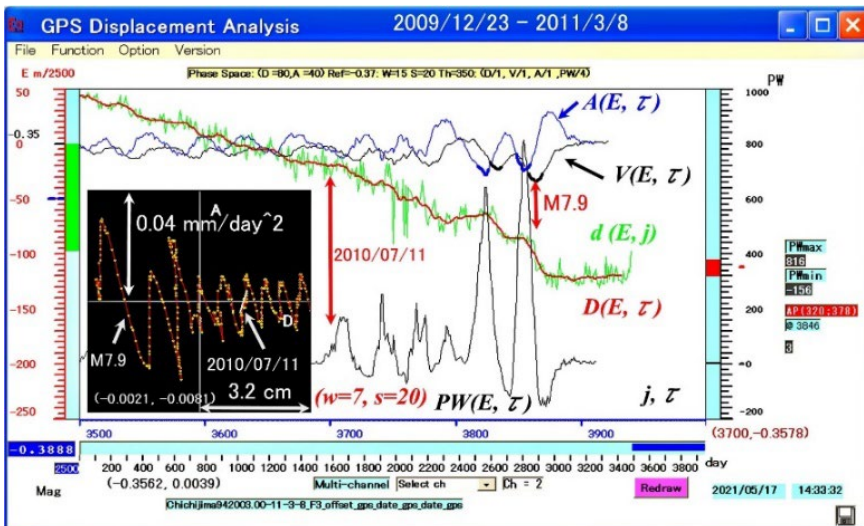
The  $PW(E, j)$  monitoring for the low-frequency  $D(E, \tau)$ ,  $V(E, \tau)$ , and  $A(E, \tau)$  accompanies the anomaly-onset-detection delay in real-time  $j$ . However, the delay allowance depends on the detecting objectives. For example, the unexpected  $V(E, j)$  and  $A(E, j)$  detection time in Fig. 6d was  $j = 3847$  (5 Dec 2010). In contrast, it was  $j = 3869$  (27 Dec 2010) with  $w = 15$  and  $s = 40$  in Fig. 6g. The detection date, 5 Dec, may help predict the imminent M7.9 event on 22 Dec. However, 27 Dec and the preceding  $D(E, \tau)$  trend-change detections were for the Tohoku M9 events on 11 Mar 2011. Automated power monitoring with multiple frequencies and thresholds for any abnormal event detection is always available.

The overriding edge pulled the subducting oceanic plate at the abnormal westward speed of  $V(E, \tau) = -0.69$  mm/day, as in Table 1. The  $D(E, \tau) - A(E, \tau)$  paths in Figs. 7a – 7d show the lunar synodic tidal force  $F(E, \tau)$  loading by a segmented equation,  $F(E, \tau) \approx A(E, \tau) \approx K \times D(E, \tau)$  with a constant  $K$  (positive or negative). The subducting oceanic plate has a steady westward movement. The periodic tidal force loading on the plate motion shows negative  $K$  under no other external force loading. A standard tidal force loading with negative  $K$  stands for no external force except the tidal force on the plate motion. The standard tidal force must have an appropriate range of  $\Delta D(E, \tau)$  and  $\Delta A(E, \tau)$  on the  $D(E, \tau) - A(E, \tau)$  path like the ranges before the trend change on 2010/07/11 in Figs. 7a – 7d.

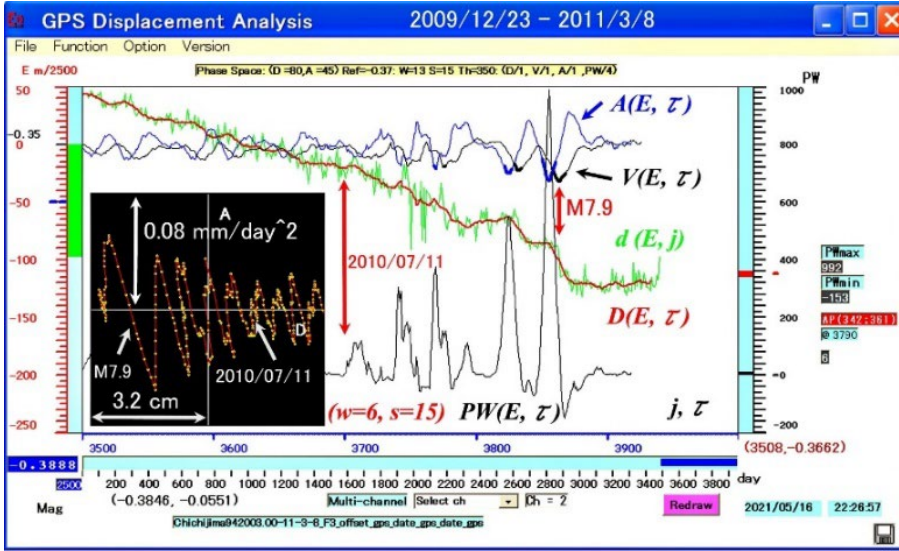
(a)



(b)



(c)



(d)

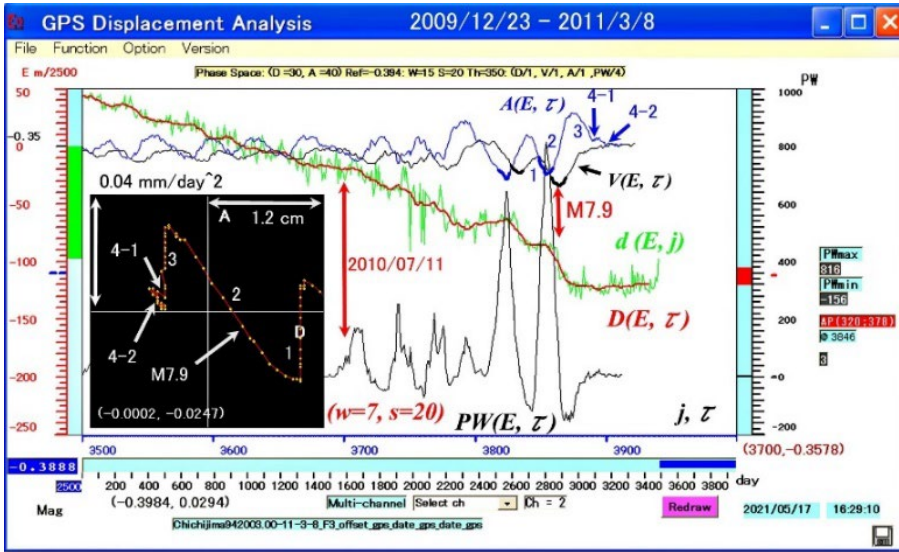


Figure 7.  $D(E, \tau) - A(E, \tau)$  path for Fig. 6b

Reproduced from reference [8]. (a) The  $D(E, \tau) - A(E, \tau)$  path with  $w = 7$  and  $s = 20$  at Chichijima station for Fig. 6b. (b) The  $D(E, \tau) - A(E, \tau)$  path with a segment equation of  $A(E, \tau) \approx K \times D(E, \tau)$  for Fig. 6b. The westward trend-change at arrow 2010/07/11 is in a white segment line. (c) The  $D(E, \tau) - A(E, \tau)$  path with  $w = 6$  and  $s = 15$  shows a higher frequency structure of  $A(E, \tau)$  in the white segment. (d) A magnified  $D(E, \tau) - A(E, \tau)$  path for the last three months before the Tohoku M9.

Figure 7b shows a linear segment of the  $D(E, \tau) - A(E, \tau)$  path as a white line. The linear change is  $(\Delta D(E, \tau), \Delta A(E, \tau)) = (-0.0021, -0.0081)$  in (m, mm/day<sup>2</sup>) from  $A(E, \tau) = 0.0039$  mm/day<sup>2</sup> at  $\tau = 3681$  on 22 Jun 2010, as shown below the time scale  $(-0.3562, 0.0039)$  in (m, mm/day<sup>2</sup>). Thus,  $A(E, \tau) \approx K \times D(E, \tau)$  has  $K = 0.0039$  /day<sup>2</sup> because  $K = \Delta A(E, \tau) / \Delta D(E, \tau) = 3.85^{-2}$ /day<sup>2</sup>. The  $(3700, -0.3578)$  in  $(\tau, m)$  below the  $PW$  scale shows the  $D(E, \tau)$  reading at the trend change. The segment in a white line in Fig. 7b preceded the trend change at label 2010/07/11. It had a positive  $K$  in  $A(E, \tau) \approx K \times D(E, \tau)$ , suggesting that the standard tidal loading began to couple with the east coast bulge. Thus,  $K$ ,  $\Delta D(E, \tau)$ , and  $\Delta A(E, \tau)$  are quantitative indicators of external force coupling with the standard tidal loading.

Figure 7c shows that an insufficient synodic tidal loading on the segment appears on the  $D(E, \tau) - A(E, \tau)$  path in a higher frequency resolution with  $w = 6$  and  $s = 15$ . A fine structure of the white line segment (in Fig. 7b) is a three-



segmented  $A(E, \tau)$  at arrow 2010/07/11. The first  $A(E, \tau)$  changes from up (eastward) to down (westward) with a positive  $K$ . The second changes opposite the first, from westward to eastward, having a negative  $K$ . The third  $A(E, \tau)$  is the same as the first with a positive  $K$ . The positive  $K$  shows that the plate's westward movement had the standard tidal loading constrained by the overriding Tohoku eastern edge bulging. A similar fine structure preceding the trend change shows a repeated constraint by the east coast bulge coupling with the westward movement.

Figure 7d shows four linear segments of the  $D(E, \tau) - A(E, \tau)$  path, magnified in indexed order for Fig. 6b. The  $A(E, \tau)$  has the corresponding indexes. The path segments are the last part of the M9 EQ genesis process. Each segment has the index number, starting time  $\tau$ , ( $\Delta D(E, \tau)$  mm,  $\Delta A(E, \tau)$  mm/day<sup>2</sup>), and  $K$  in  $A(E, \tau) \approx K \times D(E, \tau)$ . Segment 4 has two sub-portions, 4-1 and 4-2. Last segment 4-2 ends at  $\tau = 3913$  on 9 Feb 2011 because  $j = 3940$  is 8 Mar 2011 ( $\tau = 3940 - w - s$ ).

Segment	$\tau$	Date	( $\Delta D(E, \tau)$ mm, $\Delta A(E, \tau)$ mm/day <sup>2</sup> )	$K$ (1 /day <sup>2</sup> ).
1	3844	2 Dec 2010	(0.1 mm, -0.0330 mm/day <sup>2</sup> )	$K = -0.0330$ /day <sup>2</sup>
2	3854	12 Dec 2010	(-8.7 mm, 0.0434 mm/day <sup>2</sup> )	$K = -0.0050$ /day <sup>2</sup> .
3	3878	5 Jan 2011	(-0.2 mm, -0.0247 mm/day <sup>2</sup> )	$K = 0.1235$ /day <sup>2</sup> .
4-1	3890	17 Jan 2011	(-1.6 mm, 0.0034 mm/day <sup>2</sup> )	$K = -0.0213$ /day <sup>2</sup> .
4-2	3894	21 Jan 2011	(1.5 mm, -0.0068 mm/day <sup>2</sup> )	$K = -0.0453$ /day <sup>2</sup> .

The oceanic plate has the unusual tidal force coupling of 33 days in segments 1 and 2. Constant  $K$  in segment 2 is minimal, indicating no effective tidal force loading. It suggests that the tidal loading had an avalanche-like effect on the plate's westward motion. The bulging eastern edge pulled the plate westward with the highest velocity that triggered the M7.9 at  $\tau = 3864$  on 22 Dec 2010, the arrow on the  $D(E, \tau) - A(E, \tau)$  path at  $A(E, \tau) \approx 0$ . Segment 3 then shows the abnormally high external force loading with  $K = 0.1235$  /day<sup>2</sup> on the standard tidal loading, indicating that the bulge pulling has a sudden deceleration. Segment 4-1 recovers the standard tidal loading for only five days. Segment 4-2 shows the east coast moving eastward by 1.5 mm to prepare the rupturing process of the megathrust EQ, as in Fig. 4c.

## 6 Automatic detection of anomalies

Automatic real-time detection of the anomalies comparable to the amplitudes of the observed fluctuations in  $\{c\}$  requires power monitoring [8, 32–38]. The power is the time-rate change of the kinetic energy defined by  $PW(c, \tau) = V(c, \tau) \times A(c, \tau)$  with some variations [32]. For the real-time monitoring at the current time  $j = \tau + w + s$  in  $A(c, \tau)$ , the power is  $PW(c, j) = V(c, j) \times A(c, j)$ . The power at time  $j$  is

$$PW(c, j) = V(c, j) \times A(c, j) = \frac{1}{s} KE(c, j) \times \left( 1 - \frac{V(c, j-s)}{V(c, j)} \right). \quad (5)$$

The  $KE(c, j)$  is the kinetic energy, defined as the squared of  $V(c, j)$ . Velocity  $V(c, j)$  extracts mainly the fluctuations of period  $2s$  for which  $D(c, j)$  and  $D(c, j-s)$  will have the opposite sign to each other. The  $KE(c, j)$  magnifies the relative velocity change in Eq. (5) parentheses. Thus, power  $PW(c, j)$  becomes maximum near either troughs or peaks of the periodic fluctuations of  $2s$  in  $A(c, j)$ . The larger the amplitude of  $A(c, j)$  with the localized  $2s$  becomes, the larger  $PW(c, j)$ . Thus, any anomaly becomes the corresponding large  $PW(c, j)$ . A predetermined threshold detects the rising and falling  $PW(c, j)$ , which becomes higher than the threshold level and gives the anomaly-onset time. The threshold level

may automatically adopt the  $PW(c, j)$ 's maximum amplitude during the standard condition. A detailed example of power monitoring is in a GPS displacement analysis [8]. Replacing  $D(c, \tau)$  with any noisy signal or time series data observed by physical systems, we can apply  $PW(c, j)$  to automatic anomaly detections.

## 7 A strain-energy cycle during the significant and megathrust EQ genesis processes

Moving sums of  $2s d(INT, j)$ s and  $2s d(DEP, j)$ s express the density of strain energy in a selectable region [6, 7]. They are also the functions of noise-free principal stress components. Significant EQ genesis processes in every mesh of about  $4^\circ$  by  $5^\circ$  in Japan accompany the strain energy accumulation and release cycles [6, 7, 11–14]. Their normalized cycles with the past maximums are  $NCI(m, 2s)$  for  $2s d(INT, j)$ s and  $NCD(m, 2s)$  for  $2s d(DEP, j)$ s. The  $NCI(m, 2s)$  is inversely proportional to seismic activity. The activity is quiet if the EQ's emerging average rate is slow. The  $NCD(m, 2s)$  is proportional to an averaged seismic depth. If it is large, the seismic activity is deep. The  $NCD(m, 2s)$  and  $NCI(m, 2s)$  are scale-dependent tools to detect the critical stress (strain energy) build-up in the B upper crust and the D-B transition region [7].

The  $NCI(m, 2s)$  and  $NCD(m, 2s)$  increase during the significant EQ genesis processes. Figure 8a shows that the strain-energy accumulations in  $NCI(m, 70)$  and  $NCD(m, 70)$  reach the quietest and deepest seismicity at about  $m = 556$  (6 Apr 1994), which is  $t = 521$  due to  $m = t + 35$ . The energy accumulation of CQKD peaks around the highest NDEP–25(t) at  $t = 528$  in Fig. 8a during CQK for the 1995 Kobe M 7.2. After reaching the peak, a rapid strain energy release into shallower seismicity began and continued until the 1995 Kobe event at  $m = 602$  (17 Jan 1995). Figure 8a shows that a new strain-energy accumulation and release process started for the 1997 Yamaguchi M6.7 (CQT) after the 1995 Kobe M7.2, and another new process began for the 2000 Tottori M7.2 (CQT). Thus, a cycle of strain energy accumulation and release repeats, as shown in  $NCI(m, 2s)$  and  $NCD(m, 2s)$ . The so-called Accelerated Moment Release (AMR) increases the background seismicity during the strain-energy release.

The  $NCI(m, w)$  and  $NCD(m, w)$  in Fig. 8a show a predictable rupture date for the large EQ. The  $NCI(m, w)$  and  $NCD(m, w)$  generally peak a few days before a significant event occurs in wide regions. Changes in the regional size,  $Mc$ , and  $w$  increase the prediction accuracy within a day. For example, Fig. 8b shows the 1995 Kobe M7.2 in the large region of  $16^\circ$ – $52^\circ$  N and  $116^\circ$ – $156^\circ$  E with  $Mc = 4$  and  $w = 30$ . The  $NCI(m, 30)$  peaks at  $m = 9892$  (14 Jan 1995, at 04:49), and  $NCD(m, 30)$  peaks at  $m = 9906$  (16 Jan 1995, at 08:53). The Kobe event occurred at  $m = 9909$  (17 Jan 2015, at 05:40). Figures 7a and 7b show that  $NCI(m, 2s)$  and  $NCD(m, 2s)$  increase to their peaks together, and then they rapidly decrease from their peaks, during which a significant shallow event occurs. If the expected event is significant and deep, like EQs in the Wadati-Benioff zone,  $NCD(m, 2s)$  keeps increasing. Figure 9 shows the event-time predictability in a cycle of strain-energy accumulation and release for the fore and main event (the 2011 Tohoku M9). The number of averages and the  $Mc$  value may change in real-time monitoring.

The final date conversion from time  $m$  becomes within a day by real-time monitoring of strain-energy accumulation and release cycles expressed by Physical Wavelets [6, 7]. The region may be near the expected epicenter area, much smaller than mesh  $4^\circ \times 5^\circ$  while reducing the  $Mc$  value. The moving sum  $2s$  may be any number  $w$ .

Automatic detection of the anomalous peak with a sharp increase and a sudden decrease requires real-time  $PW(c, j)$  monitoring in section 6 by replacing  $D(c, \tau)$  with  $NCI(\tau, 2w + 1)$ .

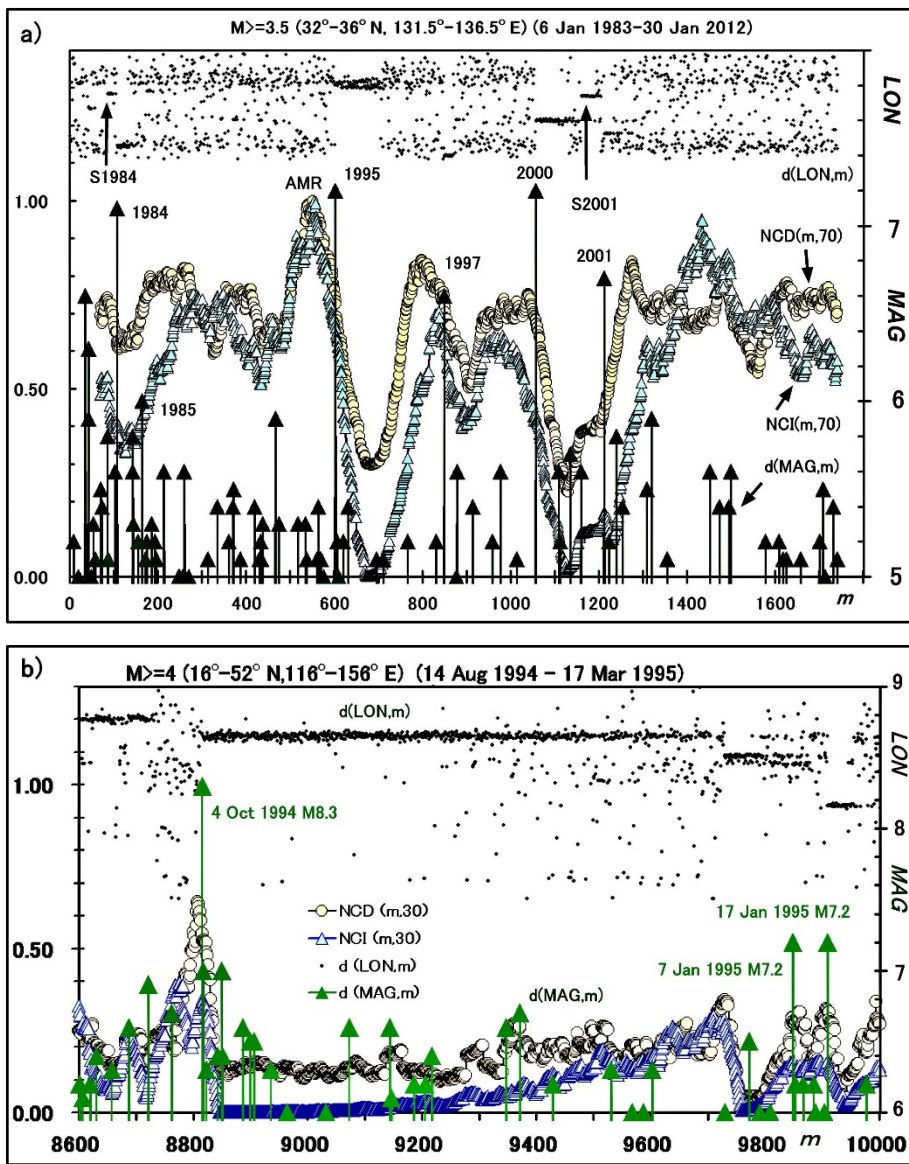


**Figure 8. Normalized strain-energy cycle on the 1995 Kobe M7.2**

Modified and reproduced from references [6, 7]. (a) The normalized strain-energy-density time series (cycle)  $NCI(m, 70)$  and  $NCD(m, 70)$  from 6 Jan 1983 to 30 Jan 2012 in the small region of  $LAT = 32^{\circ}\text{--}36^{\circ}\text{ N}$  and  $LON = 131.5^{\circ}\text{--}136.5^{\circ}\text{ E}$  as in Fig. 2a. Their time series are from shallow EQs of  $MAG \geq 3.5$  and  $DEP \leq 300$  km. The large EQs have labels on  $d(MAG, m)$  in the full-year notation. For example, two EQ swarms are S1984 and S2001, respectively. The figure axes are the same as those in Fig. 1a. A background seismicity increase, AMR, started at  $NCI(m, 70)$  and  $NCD(m, 70)$ 's peaks and continued to the 1995 Kobe M7.2. Time  $m$  has the following corresponding date:  $m = 200$  to 3 Jan 1986;  $m = 400$  to 28 Apr 1990;  $m = 600$  to 16 Jan 1995;  $m = 800$  to 26 Jun 1996;  $m = 1000$  to 28 Dec 1999;  $m = 1200$  to 8 Feb 2001;  $m = 1400$  to 27 Oct 2004;  $m = 1600$  to 15 Jul 2009. (b) The  $NCI(m, 30)$  and  $NCD(m, 30)$  from 14 Aug 1994 to 17 Mar 1995 in the large region of  $LAT = 16^{\circ}\text{--}52^{\circ}\text{ N}$  and  $LON = 116^{\circ}\text{--}156^{\circ}\text{ E}$ . Their time series are from all EQs of  $MAG \geq 4$  from JMA focus catalogs of 1983 – 1997. The strain-energy cycles show the 4 Oct 1994 M8.3, the 7 Jan 1995 M7.2, and the 17 Jan 1995 M7.2 (Kobe event). Time  $m$  has the following corresponding date:  $m = 8800$  to 27 Sept 1994;  $m = 9000$  to 5 Oct 1994;  $m = 9200$  to 9 Oct 1994;  $m = 9400$  to 21 Oct 1994;  $m = 9600$  to 22 Nov 1994;  $m = 9800$  to 30 Dec 1994.

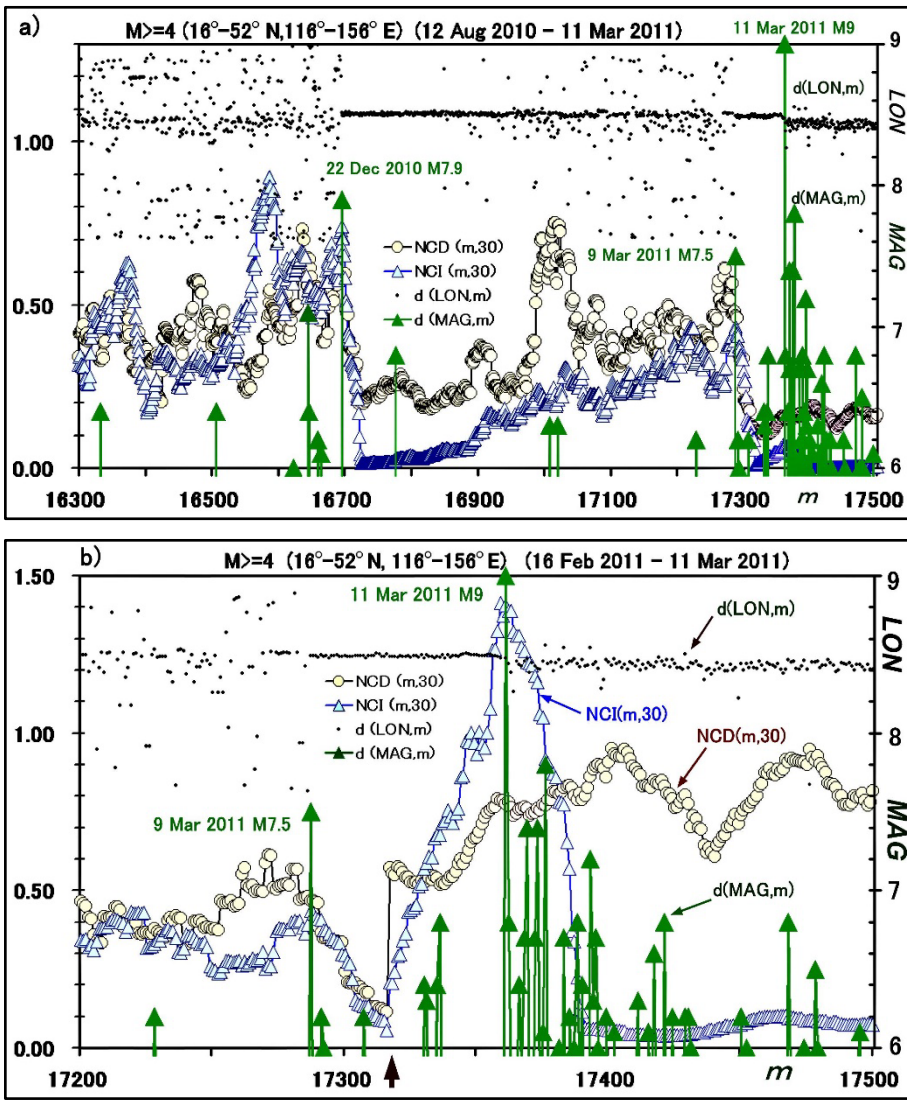


**Figure 9. Normalized strain-energy cycle on the 2011 Tohoku M9**

Modified and reproduced from references [6, 7]. (a) The normalized strain-energy-density time series (cycle) of  $NCI(m, 30)$  and  $NCD(m, 30)$  from 12 Aug 2010 to 11 Mar 2011. Their time series are the EQs of  $MAG \geq 4$  from the JMA unified focus catalogs for the region of  $LAT = 16^\circ - 52^\circ N$  and  $LON = 116^\circ - 156^\circ E$ . The figure axes are the same as those in Fig.2 and Fig.8. The 22 Dec 2010 M7.9 at  $m = 16695$  is a precursory event to the 2011 Tohoku M9, which occurred near Chichijima (an island in the Pacific Ocean), as in Fig.3. A large foreshock to the M9 event at  $m = 17287$  is the 9 Mar 2011 M7.5. Time  $m$  has the following corresponding date:  $m = 16500$  to 3 Oct 2010;  $m = 16700$  to 22 Dec 2010;  $m = 16900$  to 28 Dec 2010;  $m = 17000$  to 10 Jan 2011;  $m = 17100$  to 25 Jan 2011;  $m = 17200$  to 16 Feb 2011;  $m = 17300$  to 9 Mar 2011. (b) The normalized and magnified strain-energy cycle of  $NCI(m, 30)$  and  $NCD(m, 30)$  from  $m = 17200$  (16 Feb 2011 at 02:23) to 17500 (11 Mar 2011 at 22:35). The  $NCI(m, 30)$  and  $NCD(m, 30)$  are respectively magnified by 20 and 5 times after  $m = 17317$  (9 Mar 2011 at 16:56) pointed with the up-arrow on the  $m$  axis. The peaks for  $NCI(m, 30)$  and  $NCD(m, 30)$  are at  $m = 17359$  (11 Mar 2011 at 13:12) and  $m = 17358$  (11 Mar 2011 at 10:41), respectively. The 11 Mar 2011 M9 (the 2011 Tohoku M9) occurred at  $m = 17361$  (11 Mar 2011 at 14:46). Time  $m$  has the following corresponding date and time:  $m = 17300$  to 9 Mar 2011 at 13:04;  $m = 17400$  to 11 Mar 2011 at 16:36.

### Concluding summary

This article is an updated summary of Japanese EQ prediction patents [6, 14], a combined summary of two references [7, 8]. The patents claim the real-time prediction of the significant and megathrust EQs, based upon the EQ genesis processes observed by Japan's seismograph [4] and GPS [5] networks with Physical Wavelets [6-8].



An EQ event is a virtual particle of unit mass that emerges in the EQ source parameter  $c$ -coordinate space. The coordinates are  $c = LAT$  (latitude),  $LON$  (longitude),  $DEP$  (focal depth),  $INT$  (inter-event time), and  $MAG$  (magnitude) to be acquired by an online seismic network or catalogs. The consecutive events in mesh size of about  $4^\circ \times 5^\circ$  throughout Japan draw the non-derivative (stochastic) trajectory in the space, whose component is time series  $\{c\}$  with position  $d(c, m)$  at chronological event index time  $m$ . To reduce the stochastic noise, a selection of  $MAG \geq Mc$  ( $Mc \approx 3.5$ ) is imperative for observing scale-dependent EQ phenomena [6, 7, 11–14, 21–24]. Physical Wavelets quantify a noise-free trajectory by a periodic equation of  $F(c, \tau) \propto A(c, \tau) \approx -K(c) \times D(c, \tau)$  at the index time  $\tau$ . The  $F(c, \tau)$ ,  $A(c, \tau)$ ,  $K(c)$ , and  $D(c, \tau)$  are restoring force, acceleration, a positive constant  $K(c)$ , and displacement, respectively. The  $A(c, \tau)$  is a function of three principal stress components in the mesh.  $K(c)$  is a weak function of time  $\tau$ . The unique trajectories approaching significant and megathrust EQ positions in the  $c$ -coordinate space are the EQ genesis processes named CQK and CQT.

The CQK and CQT show the phase inversion between  $A(DEP, \tau)$  and  $A(INT, \tau)$  with the negative amplitude of  $A(MAG, \tau)$  weeks and months before the event ruptures. The periodic equation predicts the fault size and movement, the rupture time, and the focus of imminent significant and megathrust EQs.

Suppose the current time is a chronological index time  $m$ . In the real-time monitoring of CQK or CQT, the current monitoring time  $m$  is  $m = \tau + w + s$ . The  $w$  and  $s$  are to define  $D(c, \tau)$  and  $A(c, \tau)$  in Eqs. (2) – (4). The CQK and CQT accompany the strain-energy accumulation and release cycles expressed with  $NCI(m, 2s)$  and  $NCD(m, 2s)$  in the selected mesh. The same cycles appear in 60 times wider mesh size surrounding the original mesh of CQK or CQT. Monitoring  $NCI(m, 2s)$  and  $NCD(m, 2s)$  in an appropriate mesh size convert the rupture prediction event time  $\tau r$  to its date and time within a day accuracy [6, 13]. Automated detection of CQK or CQT with  $\tau r$  is available by  $PW(m, 2s)$  monitoring.

A GPS network provides daily displacements at the stations with time series  $\{c\}$  with  $d(c, m)$  at time  $m$  in days;  $c = E$  (west to east),  $N$  (south to north), and  $h$  (down to up) in right-handed  $(E, N, h)$ . The  $\{c\}$  has information on the crustal deformation and movement driven by tectonic and tidal forces. Various environmental noises in  $\{c\}$  have completely masked vital information. However, Physical Wavelets quantify the noisy deformation and movement with the  $D(c, \tau) - V(c, \tau)$  and  $D(c, \tau) - A(c, \tau)$  phase-plane path. The bulge deformation on the Tohoku area (overriding tectonic plate) was a megathrust EQ genesis process over 15 months, which generated the abnormal movement of the subducting oceanic plate by coupling the two plates with the significant fault. The abnormal paths in Figs. 6 and 7 establish a real-time prediction of the megathrust EQ and tsunami generations. Thus, observing how the oceanic plate will respond to the lunar synodic (29.5 days) tidal force loadings during the megathrust genesis processes is a key to real-time prediction.

The B-upper crust has a response to the periodic lunar tidal force loadings. For example, lunar fortnightly (14 days) force loading on the B-part expects standard unless the regional frictional failure stress state has an imminent EQ with CQK or CQT. Unusual changes from standard appear as abnormal loading in  $PW(m, 2s)$  with  $w \approx 2$  and  $s \approx 7$  about two weeks before EQs with  $MAG \geq$  about 5 [38]. Thus, along with CQK, CQT,  $NCI(m, 2s)$ , and  $NCD(m, 2s)$ , the GPS observation with the phase-plane path and  $PW(m, 2s)$  establishes a supplementary real-time prediction of the significant EQs.

A few automated prediction algorithms are available for tectonically active regions with a seismic network detecting EQs of  $M \geq$  about 3. The detection may not require completeness in the EQ magnitude-frequency relations [6, 7]. A preliminary, simplified, and automated real-time prediction system has the strain-energy cycles,  $NCI(m, 2s)$  and  $NCD(m, 2s)$ , in various mesh sizes. The system uses the GPS daily displacement analyses with the phase-plane path and  $PW(m, 2s)$  to predict the significant and megathrust EQs like heavy rain and typhoon disaster prevention warnings [6].

## Acknowledgments

The author used JMA seismic data, GPS daily displacements (F3 solutions), and a Google Earth map.

The author would like to dedicate this study to the memory of the following scientists who had mentored and inspired him to face the scientific challenges of earthquake predictions: They are Professor Keiiti Aki (3 Mar 1930 – 17 May 2005), a geophysicist; Professor Makoto Takeo (6 Apr 1920 – 23 May 2010), a physicist and his dissertation [43] advisor; Professor Gertrude Rempfer (30 Jan 1912 – 4 Oct 2011), a physicist and a member of his dissertation committee; and Professor Rikiya Takeda (27 Sept 1923 – 7 Mar 2011), a fluid engineer and his father.

## References

1. Zoback, M. D., and Zoback, M. L.: State of stress in the Earth's lithosphere, in *International Handbook of Earthquake and Engineering Seismology*, Academic Press, Amsterdam, 559–568, 2002.
2. Turcotte, D. L., and Malamud, B. D.: Earthquakes as a complex system, in *International Handbook of Earthquake and Engineering Seismology*, Academic Press, Amsterdam, 209–227, 2002.
3. Jensen, H. J.: *Self-Organized Criticality*, Cambridge Univ. Press, 1998.
4. NIED: National Research Institute for Earth Science and Disaster Resilience, High Sensitivity Seismograph Network Japan, 2022.  
<https://www.hinet.bosai.go.jp/?LANG=en,%202017>  
[https://www.data.jma.go.jp/svd/eqev/data/bulletin/index\\_e.html](https://www.data.jma.go.jp/svd/eqev/data/bulletin/index_e.html)
5. GSI: The Geospatial Information Authority of Japan, 2022.  
<https://mekira.gsi.go.jp/index.en.html>
6. Takeda, F.: Large and great earthquake prediction method, system, program, and recording medium, Japanese Patent 5798545, 2015.  
<https://www.j-platpat.inpit.go.jp/s0100>  
<https://patents.google.com/patent/JP5798545B2/en>  
The patent (130 pages and 85 figures) has two observations for the claims; Seismicity and GPS observations.
7. Takeda, F.: Large earthquake genesis processes observed with Physical Wavelets, arXiv:2201.02815, 2022.  
<https://doi.org/10.48550/arXiv.2201.02815>
8. Takeda, F.: A megathrust earthquake genesis process observed by a Global Positioning System, arXiv:2107.02799v2, 2022.  
<https://doi.org/10.48550/arXiv.2107.02799>
9. Aki, K.: A probabilistic synthesis of precursory phenomena, in *Earthquake Prediction: An International Review*, Maurice Ewing Ser., vol. 4, edited by D.W. Simpson and P.G. Richards, AGU, Washington DC, 566–574, 1981.
10. Geller, R. J., Jackson, D. D., Kagan, Y. Y., and Mulargia, F.: Earthquakes cannot be predicted, *Science*, 275 (5306), 1616-1617, 1997.
11. Takeda, F.: Extracting scale dependent earthquake property time series and precursors with physical wavelets, in 2002 Japan Earth and Planetary Science Joint Meeting, Abstracts (S046-006), 2002.  
[http://www2.jpгу.org/meeting/2002/pdf/s046/s046-006\\_e.pdf](http://www2.jpгу.org/meeting/2002/pdf/s046/s046-006_e.pdf)

12. Takeda, F.: Short term earthquake prediction with earthquake property time series and physical wavelets: An example of the 1995 Kobe earthquake, in 2002 Japan Earth and Planetary Science Joint Meeting, Abstracts (S046-P002), 2002.  
[http://www2.jpgu.org/meeting/2002/pdf/s046/s046-p002\\_e.pdf](http://www2.jpgu.org/meeting/2002/pdf/s046/s046-p002_e.pdf)
13. Takeda, F., and Takeo, M.: An earthquake predicting system using the time series analyses of earthquake property and crust motion, in Proc. 8<sup>th</sup> Experimental Chaos conf., edited by S. Baccaletti, B. J. Gluckman, J. Kurths, L. M. Pecora, R. Meucci, and O. Yordanov, AIP Conf. Proceedings Vol. 742, 140–151, 2004.
14. Takeda, F.: Earthquake prediction method, earthquake prediction system, earthquake prediction program, and recording medium, Japanese Patent 4608643, 2011.  
<https://www.j-platpat.inpit.go.jp/s0100>  
<https://patents.google.com/patent/JP4608643B2/en>
15. Dieterich, J.: A constitutive law for rate of earthquake production and its application to earthquake clustering, JGR, 99, 2601–2617, 1994.
16. Takeo, M.: *Disperse systems*, Wiley-VCH, 1999.
17. Utsu, T.: Statistical features of seismicity, in International Handbook of Earthquake and Engineering Seismology, Academic Press, Amsterdam, 719–732, 2002.
18. Ogata, Y.: Statistical Models for Earthquake Occurrences and Residual Analysis for Point Processes. J. Am. Stat. Assoc., 83 (401), 9–27, 1988.  
doi: 10.1080/437 01621459.1988.10478560
19. Ogata, Y.: Space-Time Point-Process Models for Earthquake Occurrences. Ann. Inst. Stat. Math., 50 (2), 379–402, 1998. doi: 10.1023/A:1003403601725
20. Zhang, Y., Ashkenazy, Y., and Havlin, S.: Asymmetry in earthquake inter event time intervals, arXiv:2108.06137, 2021.  
<https://doi.org/10.48550/arXiv.2108.06137>
21. Jin, A., and Aki, K.: Spatial and temporal correlation between coda  $Q^{-1}$  and seismicity and its physical mechanism, JGR, 94, 14,041–14,059, 1989.
22. Aki, K.: Scale dependence in earthquake phenomena and its relevance to earthquake prediction, Proc. Natl. Acad. Sci. U.S.A. 93, 3740–3747, 1996.  
<https://www.pnas.org/content/pnas/93/9/3740.full.pdf>
23. Aki, K.: A new view of earthquake and volcano precursors, Earth Planets Space, 56, 689–713, 2004.  
<https://link.springer.com/content/pdf/10.1186/BF03353079.pdf>
24. Jin, A., Aki, K., Liu, Z., and Keilis–Borok, V. I.: Seismological evidence for the brittle–ductile interaction hypothesis on earthquake loading, Earth Planets Space, 56, 823–830, 2004.
25. Jin, A., and Aki, K.: High–resolution maps of Coda  $Q$  in Japan and their interpretation by the brittle–ductile interaction hypothesis, Earth Planets Space, 57, 403–409, 2005.
26. Kikuchi M., and Kanamori, H.: Rupture Process of the Kobe, Japan, Earthquake of Jan. 17, 1995, Determined from Teleseismic Body Waves, J. Phys. Earth, 44, 429–436, 1996.
27. JMA: Japan Metrological Agency, 2021.  
<https://www.data.jma.go.jp/svd/eqev/data/mech/cmt/top.html>

28. Zhao, D., and Negishi, H.: The 1995 Kobe earthquake: Seismic image of the source zone and its implications for the rupture nucleation, *JGR*, 103(B5), 996–9986, 1998.
29. Ide, S.: Source process of the 1997 Yamaguchi, Japan, earthquake analyzed in different frequency bands, *GRL*, 26(13), 1973–1976, 1999.
30. Ohmi, S., and Obara, K.: Deep low-frequency earthquakes beneath the focal region of the Mw 6.7 2000 Western Tottori earthquake, *GRL*, 29(16), 1807, 10.1029/2001GL014469, 2002.
31. Utsu, T.: Relationships between magnitude scales, in *International Handbook of Earthquake and Engineering Seismology*, Academic Press, Amsterdam, 733–746, 2002.
32. Takeda, F., The detection apparatus of motion changes, Japanese Patent 2787143, 1998.  
<https://www.j-platpat.inpit.go.jp/s0100>
33. Takeda, F., Blood pressure measurement apparatus and associated method, United States Patent 5,425,372, 1995.  
<http://patft.uspto.gov/netahtml/PTO/index.html>
34. Takeda, F., Blood pressure measurement apparatus and associated method, United States Patent 5,626,141, 1997.  
<http://patft.uspto.gov/netahtml/PTO/index.html>
35. Takeda, F., Okada, S., Imade, M., and Miyauchi, H: Diagnosing abnormal operating conditions of rotational machineries and machine tools with physical wavelets, in *Proc. SPIE 4222, Process Control and Inspection for Industry*, 417-426. 2000.
36. Takeda, F.: New real time analysis of time series data with physical wavelets, in *Proc. 3<sup>rd</sup> Ex. Chaos Conf.*, edited by R. Harrison, W. Lu, W. Ditto, L. Pecora, M. Spano, and S. Vohra, World Scientific, 75–79, 1996.
37. Takeda, F.: A new real–time signal analysis with wavelets and its possible application to diagnosing the running condition of vehicles on wheels, *JSME Inter. J. Ser. C*, 37(3), 549–558, 1994.  
doi: 10.1299/jsmec1993.37.549
38. Takeda, F.: Short-term earthquake prediction with GPS crustal displacement time series and Physical Wavelets: Tottori and Akinada earthquakes, in *2002 Japan Earth and Planetary Science Joint Meeting, Abstracts (S046-001)*, 2002.  
[http://www2.jpgu.org/meeting/2002/pdf/s046/s046-p001\\_e.pdf](http://www2.jpgu.org/meeting/2002/pdf/s046/s046-p001_e.pdf)
39. JMA: Japan Meteorological Agency ([jma.go.jp](http://jma.go.jp)), 2022.  
<https://www.data.jma.go.jp/svd/eqev/data/higai/higai1996-new.html#higai1996>
40. Honda, R., Aoi, S., Morikawa, N., Sekiguchi, H., Kunugi, T., and Fujiwara, H.: Ground motion and rupture process of the 2003 Tokachi-oki earthquake obtained from strong motion data of K-NET and KiK-net, *EPS*, 56, 317–322, 2004
41. Panet, I., Bonvalot, S., Narteau, C., Remy, D., and Lemoine, J.: Migrating pattern of deformation prior to the Tohoku-Oki earthquake revealed by GRACE data, *Nature Geoscience*, 11, 367–373, 2018.
42. Tsuboi, S., and Nakamura, T.: Sea surface gravity changes observed prior to March 11, 2011 Tohoku earthquake, *Physics of the Earth and Planetary Interiors*, 221, 60–65, 2013.
43. Takeda, F.: Selective reflection of light at a solid-gas interface and its application, Portland State Univ., 1980.  
[https://pdxscholar.library.pdx.edu/open\\_access\\_etds/838/](https://pdxscholar.library.pdx.edu/open_access_etds/838/)

## Appendix

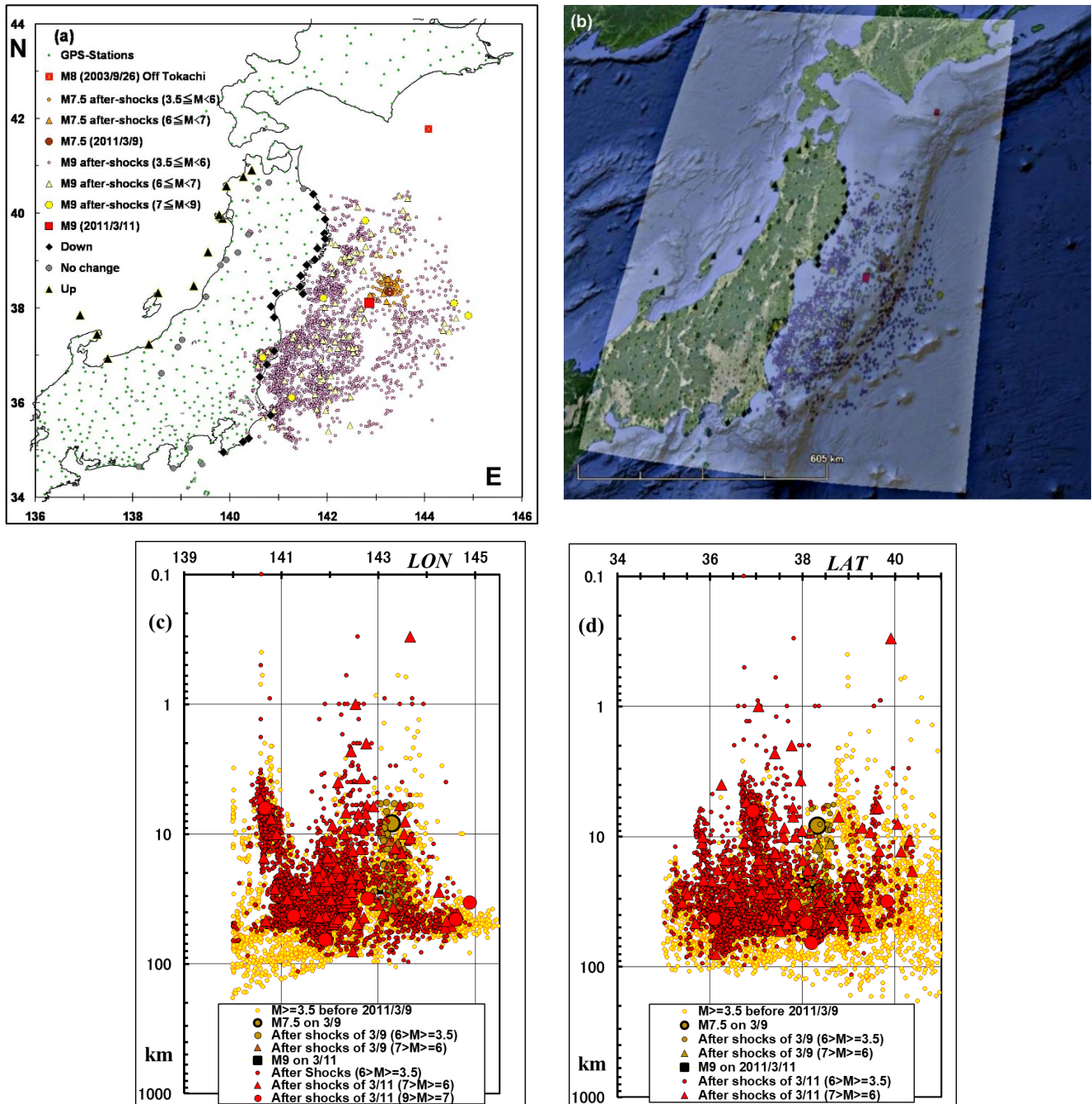


**Figure A1. Foreshocks and aftershocks of the 2011 Tohoku M9 EQ**

Modified and reproduced from references [6, 7]. (a) The EQ source parameters are from the JMA's unified focus catalogs. The EQ's magnitude  $M$  is JMA's magnitude. The M7.5 (2011/3/9) EQ is a foreshock of the Tohoku M9 EQ (2011/3/11). The M9's focus and focal mechanism were (38.1006°N, 142.8517°E, 24 km) and the reverse faulting of (STR = 193°, DIP = 10°, SLIP = 79°). Aftershocks shown in the figures are until 29 Apr 2011, and the total event number is 3634. Another significant EQ in this area was the off Tokachi M8 (2003/9/23) EQ. The vertical co-seismic displacements on 11 Mar 2011, over the 500 km distance, are the downward (Down), upward (Up), and no change (No change) displacement at each GPS station. (b) A Google Earth map with Fig. A1a overlaid. (c) The EQ focus depth,  $d$  ( $DEP, m$ ) km, in logarithmic scale and  $LON$  (longitude) distribution. The EQs before M7.5 (2011/3/9) on 9 Mar 2011 are from 1 Jan 1997 to 9 Mar 2011 (one before M7.5), and the total number is 8341. (d) The depth and  $LAT$  (latitude) distribution.